https://doi.org/10.5194/egusphere-2026-3025
Preprint. Discussion started: 26 June 2026


# Transport Efficiency of Turbulent Parcel in the Marine Boundary Layer and Its Implications for Droplet Activation in Marine Cloud Brightening

Pan Zhao[1], Jingyi Chen[1*], Yang Yang[2], Yue Jia[3] and Yang Yu[2,4]

[1]State Key Laboratory of Climate System Prediction and Risk Management, China Meteorological Administration Aerosol-Cloud and Precipitation Key Laboratory, School of Atmospheric Physics, Nanjing University of Information Science and Technology, Nanjing 210044, China
[2]State Key Laboratory of Climate System Prediction and Risk Management/Jiangsu Key Laboratory of Atmospheric Environment Monitoring and Pollution Control/Jiangsu Collaborative Innovation Center of Atmospheric Environment and Equipment Technology/Joint International Research Laboratory of Climate and Environment Change, School of Environmental Science and Engineering, Nanjing University of Information Science and Technology, Nanjing, Jiangsu, China
[3]School of Natural Sciences and Mathematics, University of Texas at Dallas, Richardson 75080, USA
[4]Department of Earth and Environmental Sciences, Faculty of Science, The Chinese University of Hong Kong, Sha Tin, Hong Kong SAR 999077, China

[*]*Correspondence to*: Jingyi Chen (jingyi.chen@nuist.edu.cn)

**Abstract.** Marine cloud brightening (MCB) has been proposed as a potential climate intervention strategy in which sea-salt aerosols are introduced into the marine boundary layer to enhance cloud albedo by increasing cloud droplet number concentrations (CDNC). However, whether turbulent motions can efficiently transport sea-surface-released aerosols to the cloud base remains a major uncertainty in evaluating MCB feasibility. This study investigates a stratocumulus case over the tropical Southeast Atlantic using large-eddy simulation (LES) coupled with the FLEXPART Lagrangian particle dispersion model to quantify turbulent parcel transport efficiency. Short-duration releases and high-LWP stages favor stronger transport of turbulent parcels to the cloud base. For parcels released at 00:00 UTC on 24 September, the peak instantaneous arrival rate reaches 3.39% within 15 min in d02, whereas it decreases to 1.86% and the peak arrival time is delayed to 17 min in d04; the corresponding cumulative arrival rate decreases from 94.16% to 79.70%. Although the mean in-cloud residence time decreases with increasing resolution, parcels with extremely long residence times become more frequent. Under the adopted activation parameterization, higher-resolution LES simulations yield higher activation fraction (AF) because they better resolve strong cloud-base updrafts, with AF ranging from 0.73-0.91 in d02 to 0.92-0.96 in d04. The AF is relatively insensitive to release duration but increases under high-LWP conditions. These results provide a process-level quantification of parcel transport, in-cloud residence time, and conditional activation, establishing a physical basis for evaluating aerosol delivery constraints in MCB applications.

https://doi.org/10.5194/egusphere-2026-3025
Preprint. Discussion started: 26 June 2026


## 1 Introduction

Marine cloud brightening (MCB) has been proposed as a potential approach to offset a portion of anthropogenic warming by introducing sea-salt aerosols into the marine boundary layer, increasing cloud droplet number concentrations (CDNC) in marine low clouds, and thereby enhancing cloud albedo (Latham, 1990; Bower et al., 2006; Latham et al., 2012; Ahlm et al., 2017; Hoffmann and Feingold, 2021; Wood, 2021). Despite growing interest, MCB remains at an early stage of development and is associated with substantial scientific uncertainties regarding both its technical feasibility and its climatic effectiveness (Diamond et al., 2022; Feingold et al., 2024; Rasch et al., 2024). Among these uncertainties, the turbulent transport of sea-surface-released aerosols to the cloud base, their residence within clouds, and their subsequent activation into droplets are especially important for evaluating whether seeding can produce an observable brightening signal (Diamond et al., 2020; Dhandapani et al., 2025).

Recent large-eddy simulation (LES) studies have shown that aerosol plumes can be transported preferentially to the cloud base by coherent updrafts, suggesting that unresolved or poorly represented transport pathways may bias estimates of brightening efficacy (Glassmeier et al., 2021; Dhandapani et al., 2025). However, most existing analyses rely primarily on Eulerian or grid-mean diagnostics, offering only limited insight on individual parcel histories, such as transport timing, cloud entry, and in-cloud residence time. Since these diagnostics cannot directly resolve parcel pathways from the near-surface layer to the cloud base, a Lagrangian framework is required to link parcel transport histories with subsequent cloud-base activation. As a result, the dynamical pathway linking surface release to cloud-base activation remains insufficiently quantified from a Lagrangian perspective.

In-cloud residence time is particularly relevant to aerosol activation because activation depends not only on whether parcels reach the cloud base, but also on whether they experience sufficiently strong and sustained supersaturation. Brief exposure to supersaturated conditions may leave a substantial fraction of parcels interstitial rather than activated, thereby reducing the effective activation fraction (AF) and weakening the cloud response (Nenes et al., 2001; VanReken et al., 2003; Peng et al., 2005; Grabowski and Wang, 2013; Chen et al., 2018). This issue is especially important for MCB, where the climatic impact depends on the efficiency of the full transport-activation chain rather than on aerosol injection alone.

A related uncertainty concerns the turbulent upward transport of parcels released near the sea surface. In practical seeding scenarios, parcels must first overcome local stabilization associated with evaporative cooling and then be lofted by boundary-layer turbulence to the cloud base (Russell et al., 1999; Wang et al., 2011; Jenkins and Forster, 2013; Prabhakaran et al., 2023; Hernandez-Jaramillo et al., 2023). Even after reaching the cloud base, activation remains sensitive to local supersaturation, updraft strength, aerosol size distribution, and residence time (Abdul-Razzak and Ghan, 2000; Fountoukis and Nenes, 2005; Xue et al., 2008; Morales Betancourt and Nenes, 2014; Hoffmann et al., 2022). These coupled dynamical

https://doi.org/10.5194/egusphere-2026-3025
Preprint. Discussion started: 26 June 2026


and microphysical controls motivate a process-oriented assessment of MCB in realistic marine stratocumulus environments (Stevens, 2002; Matheou and Teixeira, 2019).

Diamond et al. (2022) identified a key technical feasibility "off-ramp": the need to demonstrate that appropriately sized particles can be generated and transported through a real marine boundary layer, activate efficiently near the cloud base, and ultimately produce measurable optical brightening. Addressing this requirement calls for a framework that links boundary-layer transport directly to activation-relevant parcel histories. A Lagrangian analysis embedded in high-resolution meteorological simulations is therefore well suited to isolate the physical bottlenecks in the MCB pathway.

In this study, we combine LES with the FLEXPART Lagrangian particle dispersion model to examine a persistent stratocumulus case over the tropical Southeast Atlantic (SEA). Passive Lagrangian tracers released near the sea surface are used as numerical proxies for turbulent parcel transport. We quantify transport efficiency, transport timing, and in-cloud residence time under different release scenarios and model resolutions, and we further examine the potential implications of these transport pathways for cloud droplet activation at the cloud base. We therefore investigate the coupled transport-activation pathway of turbulent parcels within the marine boundary layer. Specifically, we examine (1) the transport efficiency of turbulent parcels from the near-surface layer to the cloud base and (2) how the thermodynamic histories of these turbulent parcels influence particle activation and the associated microphysical responses near the cloud base. By linking parcel transport dynamics with a simplified activation analysis, this study provides a Lagrangian-based quantification of the transport-residence-activation pathway relevant to assessing aerosol delivery to the cloud base in MCB applications.

## 2 Methods

### 2.1 Reanalysis Dataset

We use the European Centre for Medium-Range Weather Forecasts (ECMWF) Reanalysis 5th Generation (ERA5) dataset (Hersbach et al., 2020). The data cover the period from 00:00 UTC on 23 September to 00:00 UTC on 26 September 2009, with a horizontal resolution of $0.25^{\circ} \times 0.25^{\circ}$ and a 1-hour temporal resolution. This 3 d period includes model spin-up and provides the large-scale forcing for the WRF simulations. The post-spin-up period captures the LWP evolution and diurnal variability relevant to parcel transport and cloud-base activation, and is therefore sufficient for the intended analysis. ERA5 serves as the initial and lateral boundary conditions for the Weather Research and Forecasting (WRF) simulations. Additionally, its low cloud cover and liquid water path (LWP) time series are used as references for both case screening and evaluation of simulated cloud evolution.

### 2.2 Satellite observations

To evaluate the simulation accuracy and perform case selection, we use the Moderate Resolution Imaging Spectroradiometer (MODIS) Level-3 daily atmospheric product (MCD06COSP_D3, Collection 6.1) from Terra and Aqua satellites, with a

https://doi.org/10.5194/egusphere-2026-3025
Preprint. Discussion started: 26 June 2026


horizontal resolution of $1^{\circ} \times 1^{\circ}$, covering 23-25 September 2009. MODIS low cloud cover is used to evaluate ERA5 cloud fraction and assist case selection. Observed LWP spatial distributions and temporal evolution are used to evaluate the WRF simulations.

### 2.3 Case selection

We focus on the tropical SEA region in the Southern Hemisphere (approximately 15°S-10°S, 5°W-10°W). This region is one of the designated areas for MCB studies, as it hosts one of the world's major persistent and expansive stratocumulus decks (Wood, 2012; Feingold et al., 2024). The SEA is of particular interest for such research due to its relatively stable large-scale meteorological forcing and the high susceptibility of cloud albedo to aerosol perturbations (Zelinka et al., 2017; Diamond et al., 2020). It therefore represents a suitable region for investigating turbulent transport efficiency within the marine boundary layer and the mechanisms of cloud-droplet activation. We select a case where the cloud fraction from reanalysis datasets closely matches MODIS observations, thereby increasing confidence in the meteorological forcing field. Specifically, during the simulation period from 23 to 25 September, the ERA5 cloud fractions are 56.90%, 57.52%, and 52.43%, respectively, which exhibit good agreement with the MODIS observations of 57.28%, 57.32%, and 56.72%. The consistency between ERA5 and MODIS cloud fraction during 23 and 24 September justifies the selection of this period for analysis of parcel transport with a realistically represented stratocumulus cloud environment. Consequently, while the entire three-day period is simulated, our subsequent analysis primarily focuses on 23 and 24 September to leverage the most accurate meteorological forcing for the Lagrangian trajectory study.

### 2.4 WRF simulation

We use WRF version 4.6 with a four-layer one-way nested grid configuration (Skamarock et al., 2019). The horizontal grid spacings and domain extents are 2.7 km for d01 (15.04°S-9.94°S, 10.11°W-4.89°W), 900 m for d02 (12.73°S-10.99°S, 9.14°W-7.32°W), 300 m for d03 (12.33°S-11.51°S, 8.65°W-7.82°W), and 100 m for d04 (12.17°S-11.72°S, 8.46°W-8.00°W) (Fig. 1). The simulations are initialized with ERA5 reanalysis data and are driven at the lateral boundaries by ERA5 throughout the simulation period. Cloud microphysical processes are represented by the Thompson microphysics scheme (mp_physics = 8; Thompson et al., 2008). Shortwave and longwave radiation are parameterized using the Rapid Radiative Transfer Model for GCMs (RRTMG; ra_sw_physics = 4, ra_lw_physics = 4; Iacono et al., 2008). Surface and near-surface processes are represented by the Monin-Obukhov (Janjic Eta) surface layer scheme (sf_sfclay_physics = 2) and the Unified Noah land surface model (sf_surface_physics = 2; Janjić, 1994; Tewari et al., 2004). The Mellor-Yamada-Janjić (MYJ) planetary boundary layer (PBL) scheme is applied only in the outermost domain (bl_pbl_physics = 2 for d01) to represent sub-grid mixing. In contrast, the PBL scheme is turned off in the inner nested domains (bl_pbl_physics = 0 for d02, d03, and d04), where the model operates at LES scales and explicitly resolves the major turbulent motions (Janjić, 1994). To capture rapidly evolving turbulent structures and support accurate Lagrangian tracking, the model history output interval is set to 1

https://doi.org/10.5194/egusphere-2026-3025
Preprint. Discussion started: 26 June 2026


min for d02-d04 (history_interval = 1, 1, 1) and to 15 min for d01 (history_interval = 15). This temporal resolution allows us to better document the buoyancy-driven pathways of turbulent parcels and their residence times near cloud base.

### 2.5 FLEXPART-WRF turbulent parcel transport simulations

We use FLEXPART-WRF version 3.2, based on the model framework described by Brioude et al. (2013), to evaluate the transport characteristics of turbulent parcels within the marine boundary layer. FLEXPART-WRF is driven by three-dimensional meteorological fields from WRF and operates within a Lagrangian framework that represents turbulent mixing, random-walk diffusion, and vertical transport processes (Stohl et al., 2005; Jia et al., 2019). Turbulence is diagnosed using the FLEXPART-ECMWF parameterization (TURB_OPTION = 1), which estimates wind fluctuation statistics and Lagrangian time scales from WRF boundary-layer variables (Hanna et al., 1982). Vertical velocity ($w$) is derived from the mass-consistent divergence of horizontal winds (WIND_OPTION = -1) to reduce numerical inconsistencies in vertical transport (Fast et al., 2006). In FLEXPART-WRF, passive Lagrangian tracers released near the sea surface are used as numerical proxies for turbulent parcels. Parcels are released from five spatially distinct source regions (Boxes 1-5) located in the southeastern corner of the domain (Fig. 1d) to ensure spatial representativeness under the prevailing southeasterly winds over the SEA. Each box measures 5 km × 5 km, with 2 km horizontal and vertical spacing between adjacent boxes. A total of 50 000 parcels are released (10 000 per box) within 0-20 m above the sea surface, consistent with typical MCB injection heights and sufficient for Lagrangian statistics. Two release settings are considered:

(1) Release duration

Two release durations are considered: 10 min and 60 min. The 10 min experiment represents a pulse release, whereas the 60 min experiment represents a sustained release.

(2) Release timing

Releases are initiated at different phases of LWP evolution during the simulation period, including 14:00 UTC on 23 September 2009 (LWP minimum), 22:00 UTC on 23 September 2009, 00:00 UTC on 24 September 2009, 02:00 UTC on 24 September 2009 (LWP maximum), and 06:00 UTC on 24 September 2009 (Fig. 2). These time points sample distinct stages of cloud-field development and allow us to assess transport variability under different dynamical and thermodynamic conditions.

For the transport analysis, cloud base is identified as the first model level at which the cloud water mixing ratio exceeds $10^{-6}$ kg kg$^{-1}$, consistent with cloud-mask thresholds commonly used in previous WRF studies (Arbizu-Barrena et al., 2015). Parcel transport is evaluated based on the first arrival of parcels at cloud base. The temporal evolution of parcel transport is characterized by the instantaneous arrival rate, defined as the fraction of released parcels first arriving at cloud base at each time step, with the total number of released parcels fixed at 50,000 for each experiment. The cumulative arrival rate is then

https://doi.org/10.5194/egusphere-2026-3025
Preprint. Discussion started: 26 June 2026


obtained by integrating the instantaneous arrival rate over time and represents the fraction of released parcels that reach cloud base over the full analysis period. In this study, transport efficiency specifically refers to the cumulative arrival rate.

To further assess the sensitivity of parcel transport to model grid spacing, parcel releases are also conducted in domains d02-d04. To assess the implications of parcel transport for droplet formation after parcels reach cloud base, we apply a simplified single-mode activation analysis to parcels arriving at cloud base. This analysis is intended to provide activation-relevant context rather than to simulate aerosol spraying directly.

## 3 Results

### 3.1 Model Validation: Spatiotemporal Characteristics of LWP

To assess whether the nested WRF simulations provide a realistic meteorological background for the subsequent Lagrangian transport analysis, Fig. 1 shows the instantaneous LWP distribution at 02:00 UTC on 24 September 2009. In the outermost domain (d01), LWP exhibits a relatively homogeneous marine stratocumulus field, with a mean of $134.97\ \mathrm{g\ m^{-2}}$ and a maximum of $525.18\ \mathrm{g\ m^{-2}}$ within the clipped region, providing a suitable meteorological background for investigating boundary-layer turbulent parcel transport to the cloud base. With decreasing grid spacing, the LWP field becomes progressively more heterogeneous. In the innermost LES domain (d04), the LWP has a mean of $83.11\ \mathrm{g\ m^{-2}}$ and a maximum of $651.02\ \mathrm{g\ m^{-2}}$, and small-scale cloud structures and localized LWP fluctuations are more explicitly resolved, indicating that the high-resolution simulation captures finer-scale cloud heterogeneity more effectively. The refinement from kilometer-scale to LES-scale resolution improves the representation of boundary-layer turbulence and cloud structures, thereby providing high-resolution fields for Lagrangian trajectory analysis.

https://doi.org/10.5194/egusphere-2026-3025
Preprint. Discussion started: 26 June 2026


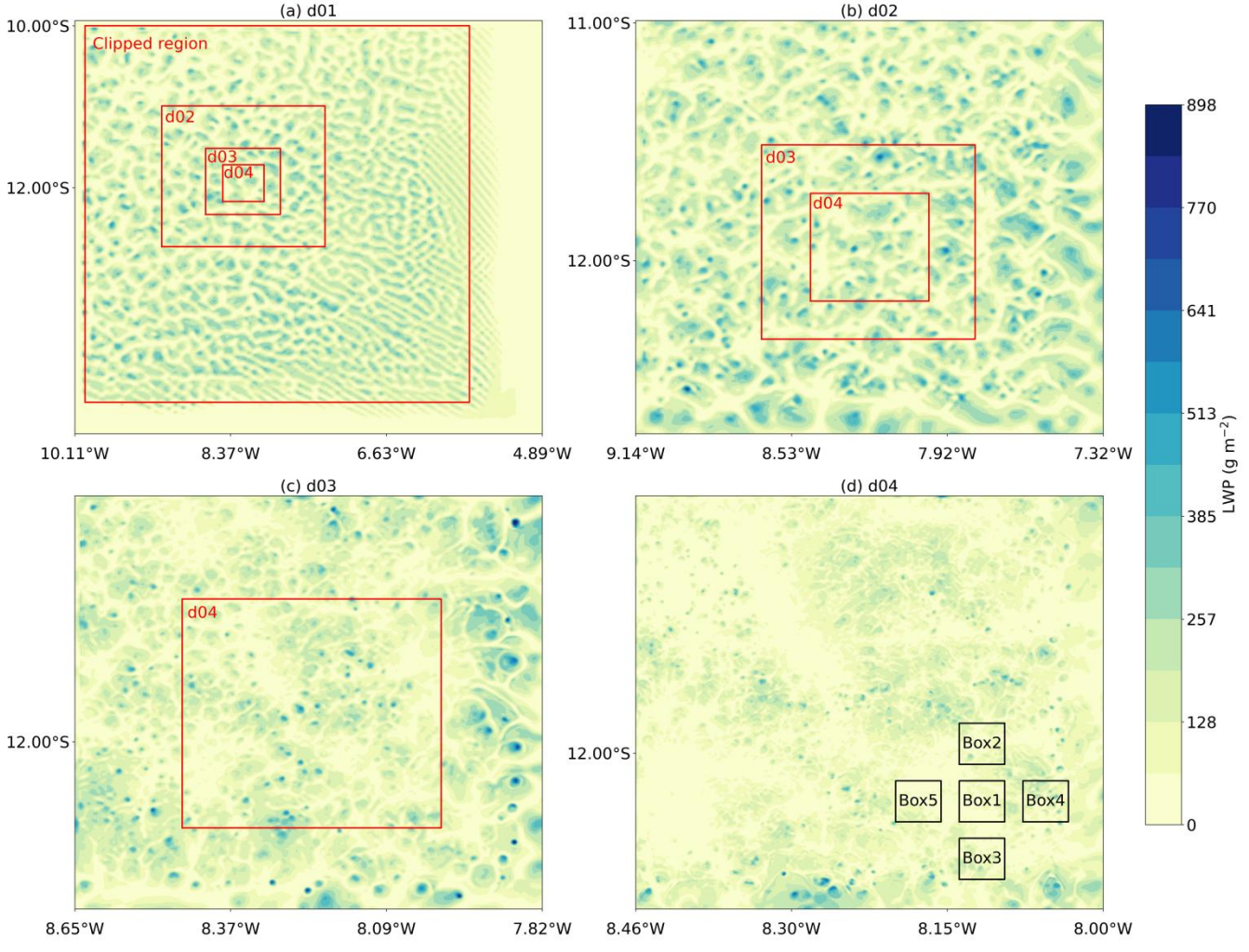


**Figure 1. Spatial distribution of instantaneous LWP (unit: g $m^{-2}$) for the nested domains d01-d04 at 02:00 UTC on 24 September 2009: (a) d01 (mean = 134.97, max = 525.18), where red boxes denote the clipped region (**14.65°S-10.00°S, 10.00°W-5.70°W**) and the boundaries of d02-d04; (b) d02 (mean = 139.80, max = 791.89), with red boxes indicating the boundaries of d03-d04; (c) d03 (mean = 120.62, max = 897.78), with the red box marking the d04 boundary; and (d) d04 (mean = 83.11, max = 651.02), where black boxes identify the Boxes 1-5 sampling areas.**

https://doi.org/10.5194/egusphere-2026-3025
Preprint. Discussion started: 26 June 2026


To evaluate whether the simulations reproduce the observed temporal evolution of cloud conditions during the selected period, Fig. 2 shows the temporal evolution of the domain-mean LWP from 10:00 UTC on 23 September to 16:00 UTC on 24 September 2009 for all nested WRF domains, alongside ERA5 reanalysis and MODIS satellite observations (available for domains d01 and d02 only). MODIS observations indicate a higher LWP on 24 September than on 23 September. The WRF simulations at kilometer-scale resolutions (d01 and d02) reproduce this day-to-day contrast. The LES-scale domains (d03 and d04) exhibit diurnal variability broadly consistent with that in the coarser-resolution domains, but with lower LWP values than those in d01-d02. In contrast, ERA5 consistently underestimates the LWP on 24 September, highlighting its limitations in representing the variability of shallow marine stratocumulus clouds.

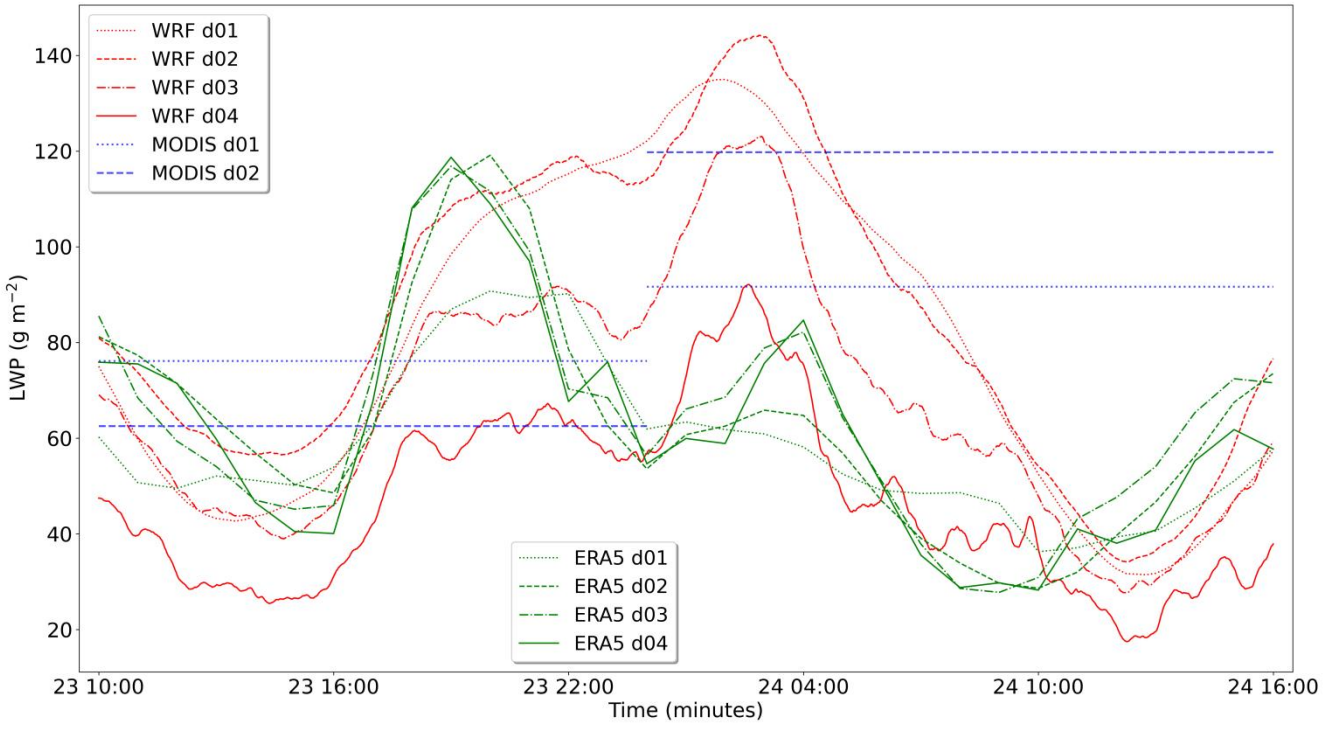


**Figure 2. Temporal evolution of the domain-mean LWP from 10:00 UTC on 23 September to 16:00 UTC on 24 September 2009, comparing the nested WRF domains (d01-d04), ERA5 reanalysis (d01-d04), and MODIS satellite observations (available for domains d01 and d02 only). Horizontal dashed lines denote the time-mean LWP for each dataset. The unit of LWP is $\mathbf{g\ m^{-2}}$.**

https://doi.org/10.5194/egusphere-2026-3025
Preprint. Discussion started: 26 June 2026


To further assess the spatial consistency of the simulated cloud field relative to observations, Fig. 3 compares daily mean LWP distributions from WRF, ERA5 and MODIS over the clipped d01 domain. For spatial consistency, WRF and ERA5 outputs are upscaled to the MODIS grid by averaging native grid points within ±0.5° of each cell center. All datasets are processed with unified daily averaging and a shared valid-data mask to enable robust statistical comparison. On 23 September, the WRF simulations yielded a median LWP of 78.20 g $m^{-2}$ (mean: 73.75 g $m^{-2}$), which agrees well with MODIS (median: 68.20 g $m^{-2}$, mean: 76.12 g $m^{-2}$). ERA5 produced a comparable median (74.40 g $m^{-2}$) and mean (73.57 g $m^{-2}$), but exhibited a noticeably narrower distribution. On 24 September, the WRF simulations (median: 87.06 g $m^{-2}$, mean: 83.29 g $m^{-2}$) showed substantially better agreement with MODIS (median: 94.85 g $m^{-2}$, mean: 91.67 g $m^{-2}$) than ERA5 (median: 56.00 g $m^{-2}$, mean: 56.61 g $m^{-2}$). These results indicate that the WRF simulations substantially reduce the low bias in ERA5 and provide a more realistic representation of marine stratocumulus LWP over the study region.

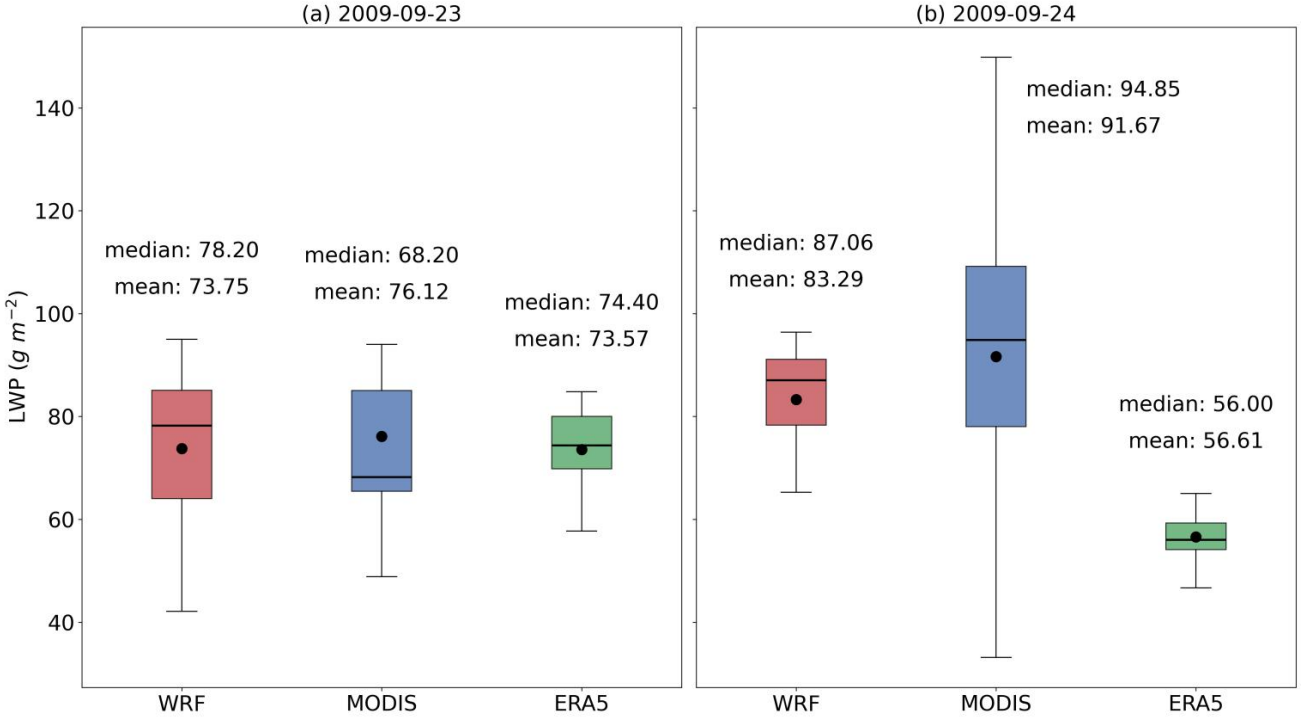


**Figure 3. Boxplots of daily mean LWP over the clipped d01 region for the WRF simulations, MODIS observations, and ERA5 reanalysis: (a) 23 September 2009. (b) 24 September 2009. Boxes represent the Interquartile Range (IQR), horizontal lines denote the medians, and black circles indicate the mean values (the corresponding statistics are labeled adjacent to each box). The unit of LWP is g $m^{-2}$.**

https://doi.org/10.5194/egusphere-2026-3025
Preprint. Discussion started: 26 June 2026


Taken together, these results indicate that the nested WRF simulations capture reasonably well the spatiotemporal variability of LWP over the study region, providing a reliable basis for subsequent analysis of boundary-layer turbulent parcel transport and its potential implications for cloud-base activation.

### 3.2 Meteorological Background and Thermodynamic Structure along Lagrangian Trajectories

To elucidate the mechanisms driving upward parcel transport, this section examines the background meteorological conditions sampled along forward trajectories from FLEXPART-WRF. The vertical structures are compared across five representative stages during the evolution of LWP described in Sect. 2.5. Figure 4 presents the vertical profiles of specific humidity ($q_v$), potential temperature ($\theta$), and turbulent kinetic energy (TKE) for these release times. Since the vertical structures of these variables are broadly similar across release durations ($t_r = 10$ min, $t_r = 60$ min), Fig. 4 only displays the representative results for $t_r = 10$ min with a 180 min tracking duration. All analyses in this section are based on results from domain d02.

In the supersaturated region (Relative humidity, $RH > 100\%$, Figs. 4a-c), turbulent parcels are predominantly distributed between approximately 510 and 1270 m in altitude. The vertical variations in $q_v$ and $\theta$ are generally small, with $q_v$ remaining in the range of $9 - 11 g\,kg^{-1}$ and $\theta$ ranging from approximately 291.5 K to 296 K, indicating a high degree of thermodynamic uniformity among the different release times. In contrast, TKE varies strongly with the stages of LWP evolution, increasing from $0.071 - 0.357\ m^2\ s^{-2}$ at 14:00 UTC on the 23rd to $0.272 - 1.384\ m^2\ s^{-2}$ at 06:00 UTC on the 24th. This enhancement suggests that, in the early morning phase following the LWP maximum (at 02:00 UTC on the 24th), intensified longwave radiative cooling at cloud top drives vigorous vertical overturning, resulting in the strongest turbulent mixing within the cloud layer.

The unsaturated layer ($RH < 100\%$, Figs. 4d-f) spans approximately 0-1500 m. Within the mixed layer (0-1000 m), $q_v$ remains consistently high, above $8.5\ g\,kg^{-1}$, reflecting the abundant moisture reservoir in the marine boundary layer. Within the mixed layer, $\theta$ is stably maintained in the range of 291-293 K. Above 1000 m, during low-LWP periods (14:00 UTC on the 23rd and 06:00 UTC on the 24th), the inversion layer is lower than during other LWP phases, as indicated by $q_v$ and $\theta$. TKE peaks near the ocean surface and decreases with height, while also exhibiting a distinct peak around 1000 m. This peak is most pronounced at 00:00 and 02:00 UTC on the 24th, corresponding to the growth and mature phases of the stratocumulus layer.

https://doi.org/10.5194/egusphere-2026-3025
Preprint. Discussion started: 26 June 2026


To clarify how parcel thermodynamic histories differ between contrasting stages of LWP evolution, we compare two representative times: 14:00 UTC on the 23rd (LWP minimum) and 02:00 UTC on the 24th (LWP maximum). Figure 5 uses kernel density estimation (KDE) probability density functions (PDFs) to characterize the differences in parcel thermodynamic properties between the two LWP stages. In the supersaturated region (Figs. 5a-d), the PDFs at 02:00 UTC extend to higher altitudes, indicating a thicker cloud during the LWP peak phase. In the unsaturated region (Figs. 5e-h), the differences between the two LWP stages are relatively small.

To identify the dynamical factor responsible for the release-time dependence of parcel transport, we further examine the vertical distribution of TKE at three key LWP stages. Figure 6 presents the KDE distributions of TKE at three key phases: 14:00 UTC on the 23rd (LWP minimum), 02:00 UTC on the 24th (LWP maximum), and 06:00 UTC on the 24th, to highlight how turbulence differs between low- and high-LWP stages. In the saturated layer (Figs. 6a-c), the maximum TKE increases much more strongly than the mean TKE across the different stages, particularly near the cloud top. This reflects enhanced cloud-top turbulent mixing during high-LWP conditions. In the unsaturated region (Figs. 6d-f), the TKE distribution displays a bimodal structure, with one peak below the cloud base ($< 200$ m) and another aloft above the cloud top (400-900 m). The maximum TKE aloft is substantially higher at 02:00 and 06:00 UTC than at 14:00 UTC, indicating a strong sensitivity of the experienced turbulence to release timing.

These results indicate that release timing modulates parcel transport by altering both the height and depth of the saturated layer and the turbulence intensity experienced along parcel trajectories. Both factors directly influence the instantaneous and cumulative transport to the cloud base and the activation conditions encountered once turbulent parcels reach the cloud base, as discussed in the following sections.

https://doi.org/10.5194/egusphere-2026-3025
Preprint. Discussion started: 26 June 2026


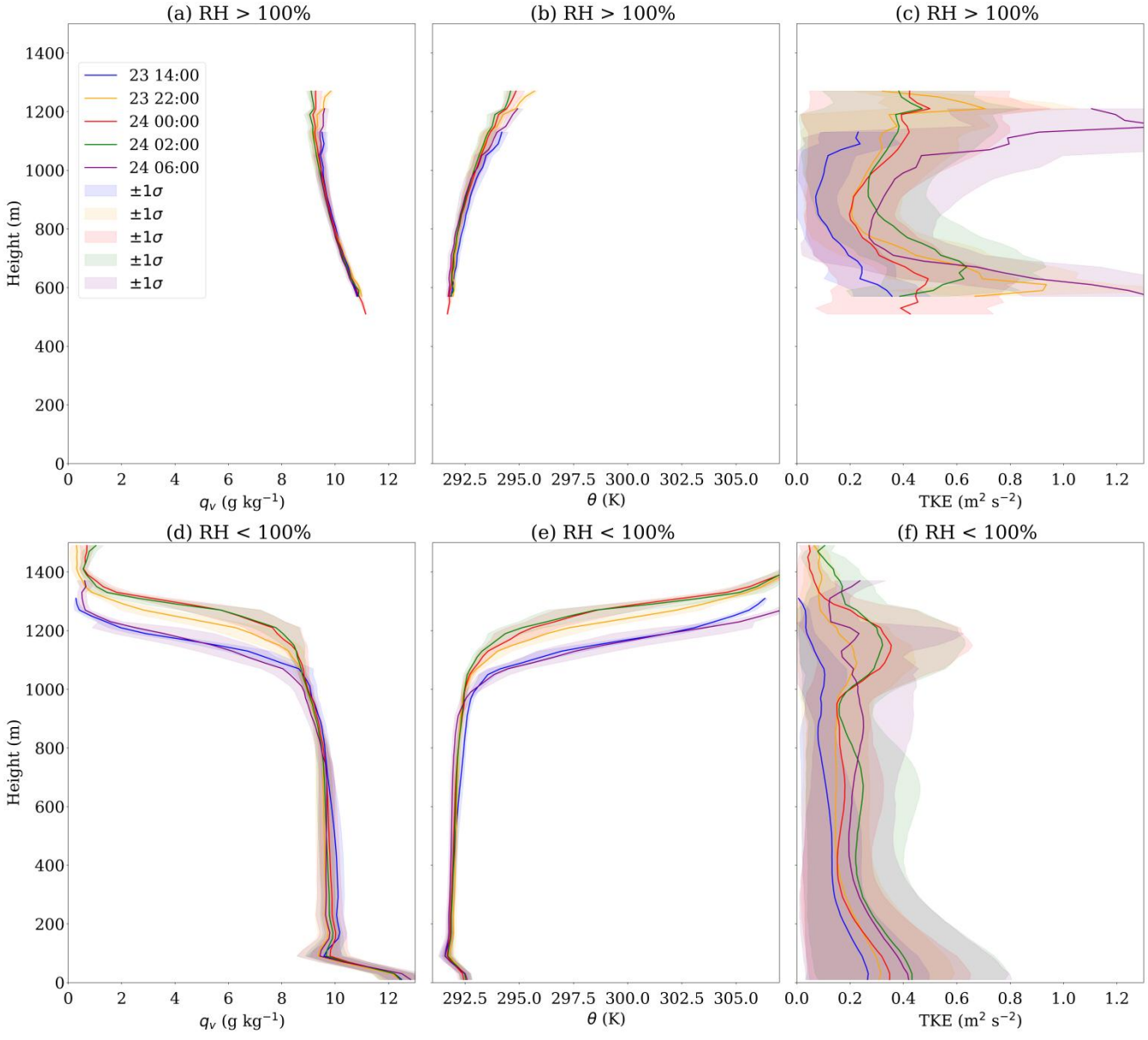


**Figure 4. Vertical profiles of background meteorological parameters for turbulent parcels at different release times ($t_r$ = 10 min, trajectory duration 180 min). (a-c) $q_v$,θ, and TKE in the supersaturated region (RH > 100%). (d-f) corresponding parameters in the unsaturated region (RH < 100%). Colors indicate different times, including blue (14:00 UTC on the 23rd), orange (22:00 UTC on the 23rd), red (00:00 UTC on the 24th), green (02:00 UTC on the 24th), and purple (06:00 UTC on the 24th). Shading represents ±1σ. The unit of $q_v$ is g kg$^{-1}$. The unit of θ is K. The unit of TKE is m$^2$ s$^{-2}$.**

https://doi.org/10.5194/egusphere-2026-3025
Preprint. Discussion started: 26 June 2026


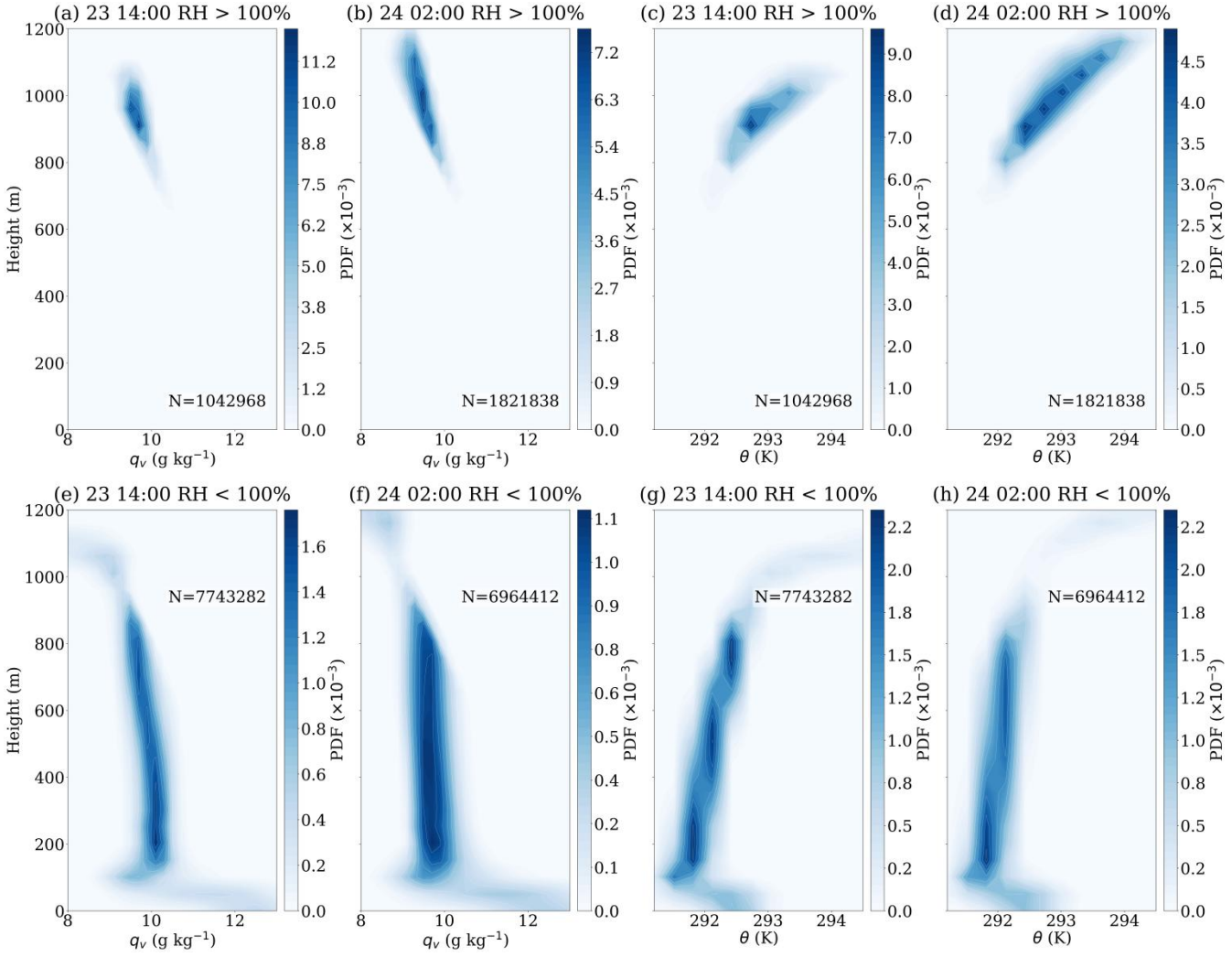


**Figure 5. KDE distributions of $q_v$ and $\theta$ as a function of height for the representative times (14:00 UTC on the 23rd and 02:00 UTC on the 24th). The upper panels show the supersaturated region ($RH > 100\%$), and the lower panels show the unsaturated region ($RH < 100\%$). N denotes the statistical sample size. The unit of $q_v$ is g kg$^{-1}$. The unit of $\theta$ is K.**

https://doi.org/10.5194/egusphere-2026-3025
Preprint. Discussion started: 26 June 2026


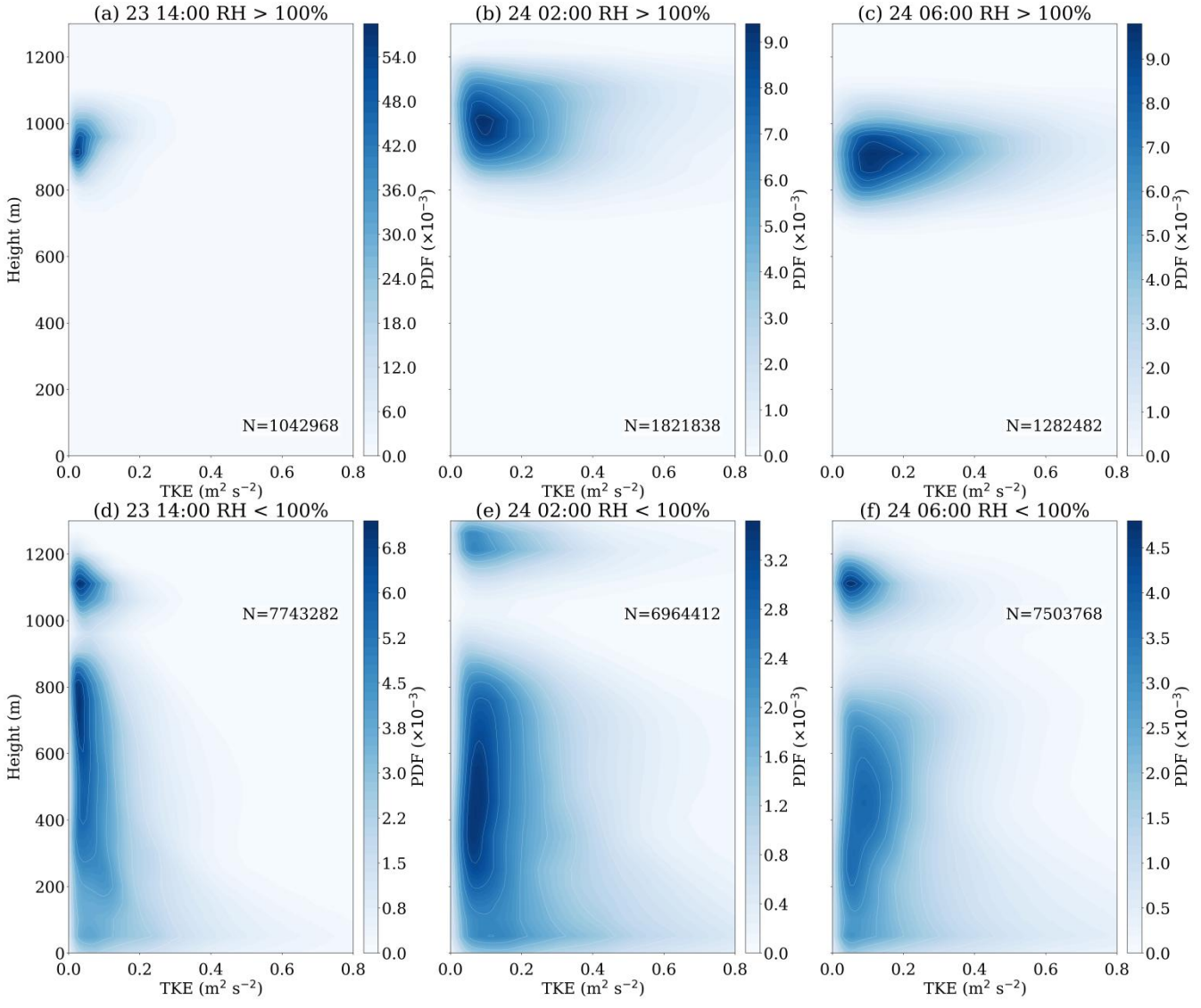


**Figure 6. PDFs of TKE as a function of height under different LWP phases (14:00 UTC on the 23rd, 02:00 UTC on the 24th, and 06:00 UTC on the 24th). The upper panels show the supersaturated region ($\mathbf{RH > 100\%}$), and the lower panels show the unsaturated region ($\mathbf{RH < 100\%}$). N denotes the statistical sample size. The unit of TKE is $\mathbf{m^2\ s^{-2}}$.**

https://doi.org/10.5194/egusphere-2026-3025
Preprint. Discussion started: 26 June 2026


### 3.3 Transport efficiency of turbulent parcels

This subsection evaluates how environmental factors during different LWP phases affect the transport of turbulent parcels to the cloud base. Figure 7 illustrates the temporal distribution of first arrival times at the cloud base within 180 min for five representative stages, with Fig. 7a showing the instantaneous arrival rate and Fig. 7b showing the cumulative arrival rate. With a fixed total number of parcels, the release duration ($t_r$) governs the instantaneous arrival rate. Short-duration releases ($t_r = 10$ min, solid lines in Fig. 7a) produce burst-like peaks of 2.45% to 3.39% within approximately 15 min, whereas long-duration releases ($t_r = 60$ min, dashed lines in Fig. 7a) show lower peak instantaneous arrival rates (1.31%-1.58%) and delayed maxima (56-62 min after release). These differences indicate that shorter release intervals result in a higher temporal density of parcels entering the flow, allowing them to be transported in more concentrated groups within coherent turbulent structures. Such releases therefore capture the peak transport capacity of active updrafts more effectively, leading to the observed burst-like arrival peaks. This difference primarily reflects the compressed release configuration. In contrast, the $t_r = 60$ min cases average transport over multiple convective cycles, resulting in a broader distribution of arrival times and lower peak instantaneous arrival rates.

The instantaneous arrival rate varies with the evolutionary phase of the LWP, yet it does not scale linearly with the LWP magnitude. Although 02:00 UTC corresponds to the LWP maximum, the highest instantaneous arrival rate occurs at 00:00 UTC on the 24th during the rapid LWP growth phase, when the peak instantaneous arrival rate reaches 3.39% for the 10-min release. In comparison, the peak instantaneous arrival rate at 02:00 UTC is slightly lower (2.96%) than at 00:00 UTC. This suggests that active boundary-layer convection provides more effective lifting than the more mature conditions during the post-peak phase. At the lower-LWP stage (22:00 UTC on the 23rd), the peak instantaneous arrival rate is lowest, with a value of only 2.45% for $t_r$ = 10 min.

Figure 7b also shows that, regardless of release time, more than 96% of parcels in d02 reach the cloud base within 180 min. A shorter release duration leads to the cumulative arrival rate curves reaching a plateau earlier. Parcels released at 00:00 UTC exhibit the steepest initial increase, approaching near-complete transport within the first 30 min, whereas those released at 14:00 UTC and in the longer-duration experiments show significant delays.

Reaching the cloud base does not guarantee droplet activation; therefore, we further examine the in-cloud residence time of parcels after cloud entry. A comparison of two contrasting phases, 14:00 UTC on the 23rd (LWP minimum) and 00:00 UTC on the 24th (the time of strongest overall transport to the cloud base), reveals distinct behaviors (Fig. 8). At 14:00 UTC, residence times increase slowly (median ~7 min at 60 min to ~20 min at 180 min, reaching ~29 min at 240 min), with few long-lived outliers, indicating weak mixing and limited in-cloud persistence. In contrast, at 00:00 UTC, stronger TKE and moisture supply produce a steeper increase (median ~25 min at 120 min, ~39 min at 180 min, and ~52 min at 240 min, with

https://doi.org/10.5194/egusphere-2026-3025
Preprint. Discussion started: 26 June 2026


Q3 up to ~70 min and numerous high-value outliers), demonstrating that the active stratocumulus growth phase both enhances overall transport to the cloud base and substantially prolongs in-cloud residence time, thereby favoring more sustained parcel-cloud interaction. Moreover, across all groups, cumulative residence time increases with simulation duration (60-240 min), with larger medians for the shorter release duration due to more concentrated cloud-base crossing, especially for the group with the strongest overall transport to the cloud base.

https://doi.org/10.5194/egusphere-2026-3025
Preprint. Discussion started: 26 June 2026


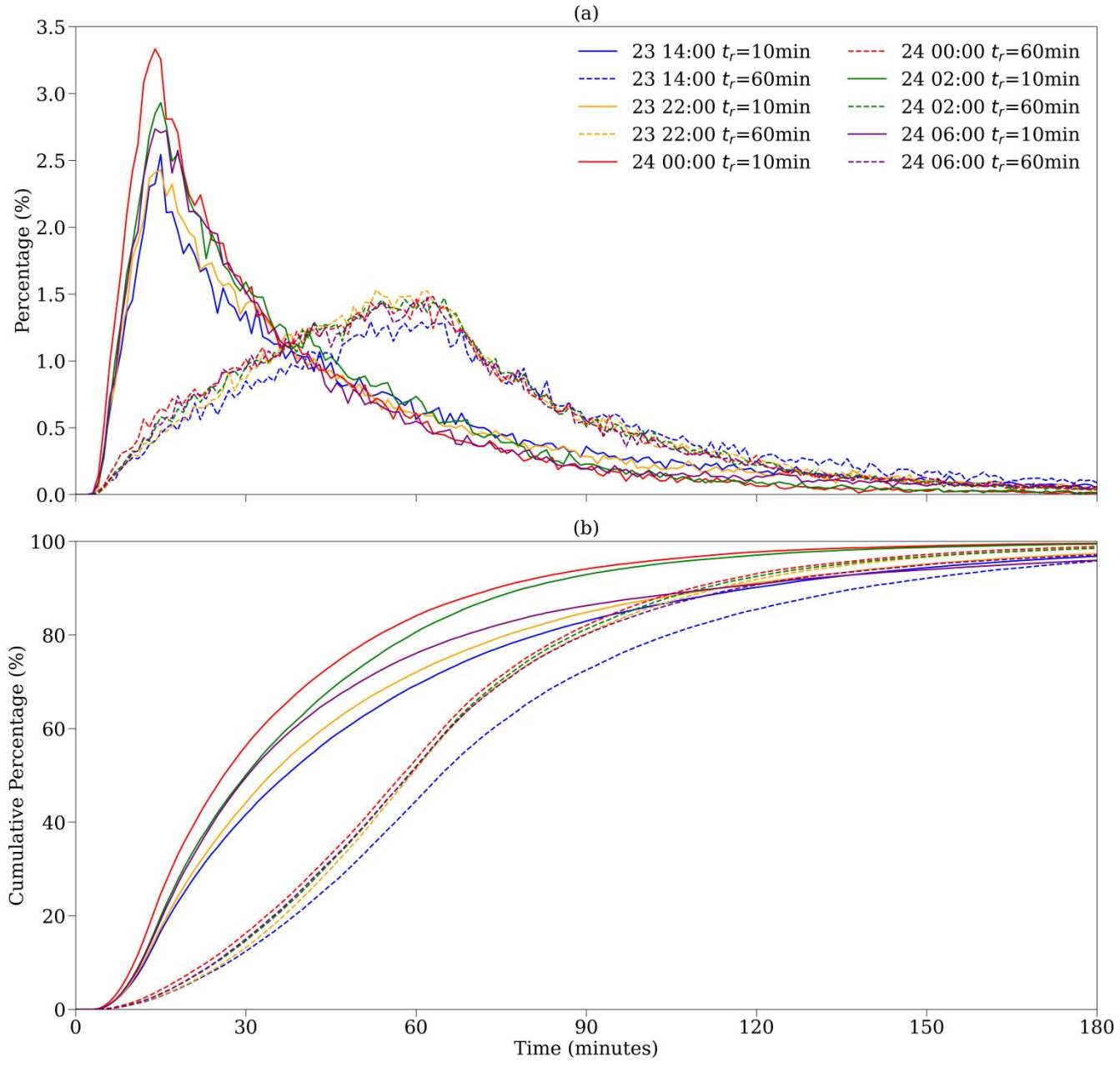


345 **Figure 7. Instantaneous and cumulative arrival of turbulent parcels at the cloud base for various release times. (a) Instantaneous arrival rate, defined as the percentage of total released turbulent parcels first arriving at the cloud base per minute. (b) Cumulative arrival rate, defined as the cumulative percentage of turbulent parcels arriving at the cloud base. Solid lines represent release duration $t_r = 10$ min; dashed lines represent $t_r = 60$ min. Colors distinguish release times: blue (14:00 UTC on the 23rd), orange (22:00 UTC on the 23rd), red (00:00 UTC on the 24th), green (02:00 UTC on the 24th), and purple (06:00 UTC on**
350 **the 24th).**

https://doi.org/10.5194/egusphere-2026-3025
Preprint. Discussion started: 26 June 2026


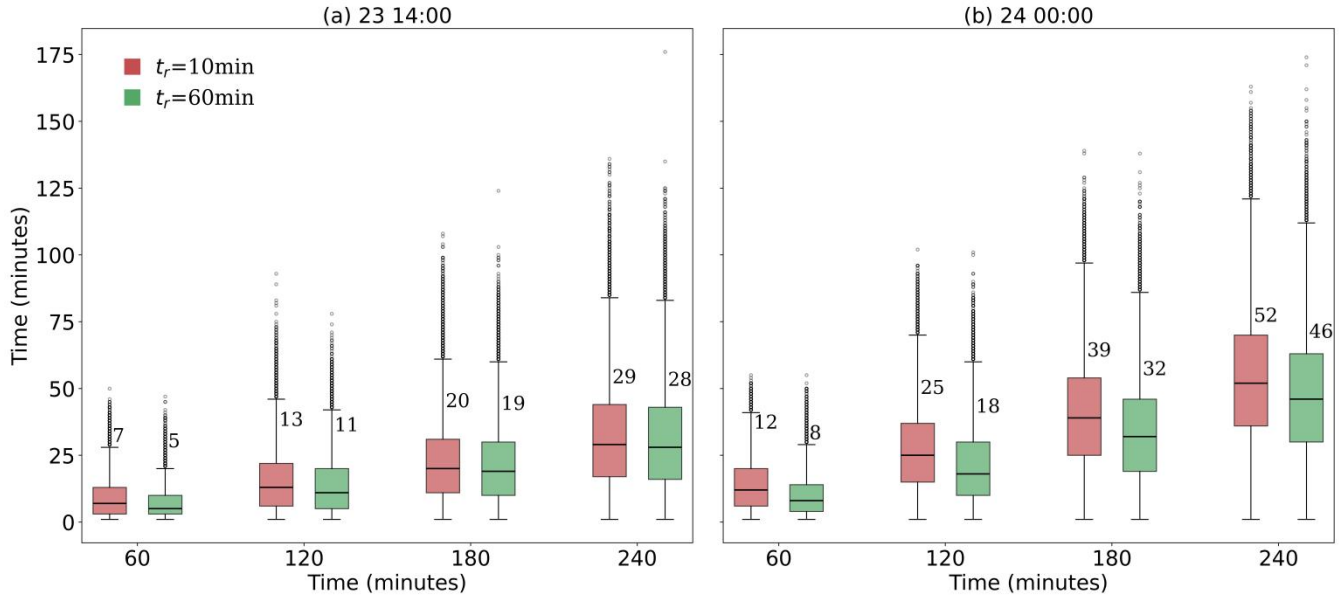


**Figure 8. Box plots of total in-cloud residence time of turbulent parcels for different simulation durations (60, 120, 180, and 240 min). (a) 14:00 UTC on the 23rd (LWP minimum), (b) 00:00 UTC on the 24th (strongest overall transport to the cloud base). Red boxes represent $t_r = 10$ min, green boxes represent $t_r = 60$ min. The central black horizontal line represents the median (numerical values are labeled above each box), while the boxes represent the IQR. Whiskers extend to the maximum and minimum values within the non-outlier range. Black open circles represent outliers, defined as data points exceeding 1.5 times the IQR from the box edges.**

The results presented above focus on domain d02 with a grid spacing of 900 m. Furthermore, we compare the simulation results from the nested domains d02, d03, and d04 to evaluate how spatial resolution influences the instantaneous arrival rate, cumulative arrival rate, and transport time of turbulent parcels from the sea surface to the cloud base, as well as their residence time within the clouds. As d04 has the smallest spatial extent and the region is dominated by southeasterly winds, turbulent parcels tend to exit the lateral boundaries relatively quickly. To ensure consistency and fair comparison across resolutions, d02 and d03 are cropped to match the geographic extent of d04, and the analysis was restricted to the first 90 minutes. During this period, at least 70% of the parcels remained within the domain for all release times, release durations, and resolutions.

As the horizontal grid spacing decreases gradually from d02 to d04, the peak instantaneous arrival rate decreases monotonically, the time of peak arrival is gradually delayed, and the cumulative arrival rate also shows a systematic reduction. For the turbulent parcels released at 00:00 UTC on 24 September ($t_r = 10$ min), the peak instantaneous arrival rates for d02, d03, and d04 are 3.39%, 2.28%, and 1.86%, respectively; the corresponding peak arrival times are 15, 16, and 17 min; and the cumulative arrival rates are 94.16%, 86.30%, and 79.70%, respectively (Fig. 9, Table 1). This pattern likely

https://doi.org/10.5194/egusphere-2026-3025
Preprint. Discussion started: 26 June 2026


reflects two factors in the present analysis: a weaker background ascent sampled along the parcel trajectories at higher resolution, and an amplification of the diagnosed differences caused by the limited analysis window and cropped domain size.

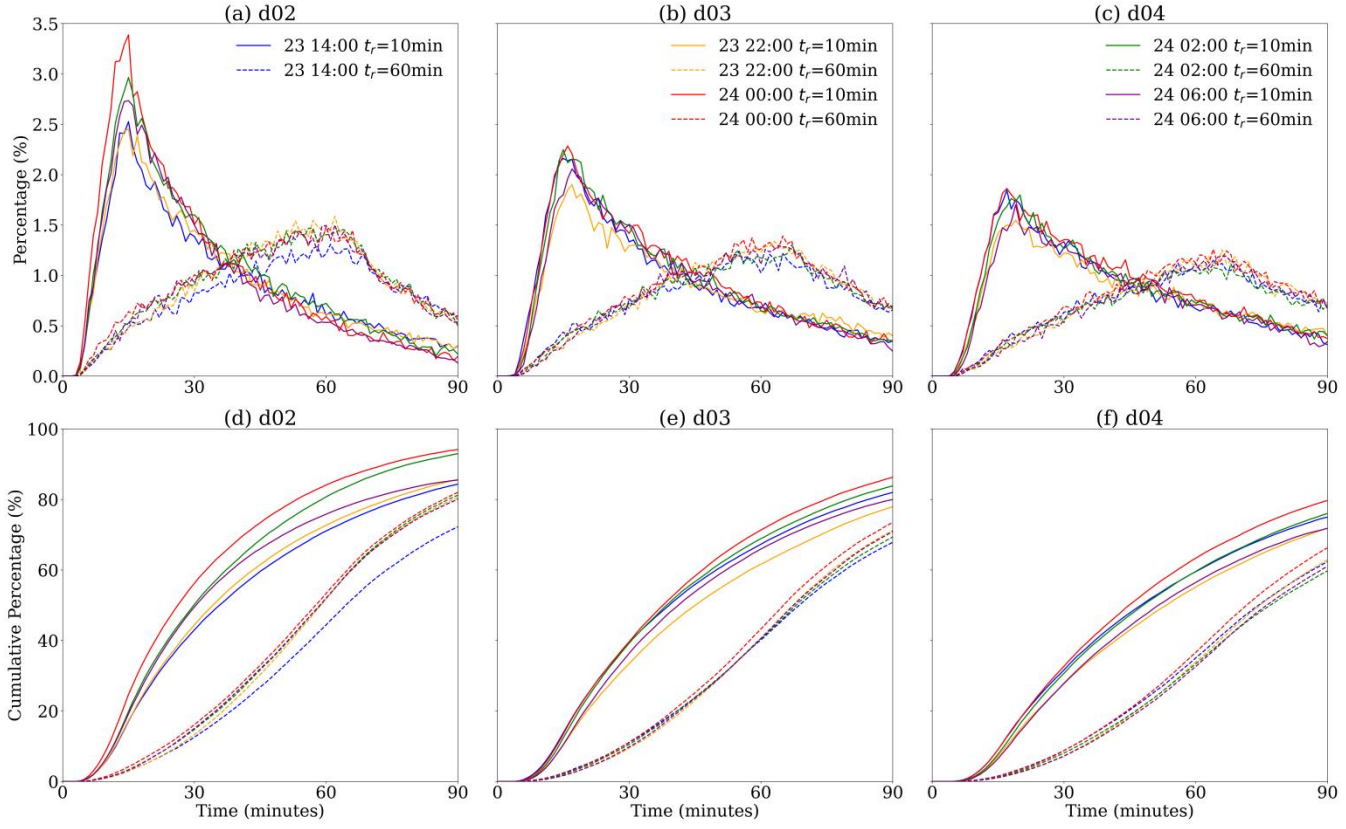


**Figure 9. Comparison of the instantaneous and cumulative arrival of turbulent parcels at the cloud base across different spatial resolutions (d02, d03, d04). Panels (a)-(c) show the instantaneous arrival rate, i.e., the percentage of turbulent parcels first reaching the cloud base per minute. Panels (d)-(f) show the corresponding cumulative arrival rate. Results are presented for five representative release times under two release configurations ($t_r = 10$ min as solid lines, $t_r = 60$ min as dashed lines). All d02 and d03 data have been cropped to the geographical extent of d04. Colors distinguish release times, blue (23rd 14:00 UTC), orange (23rd 22:00 UTC), red (24th 00:00 UTC), green (24th 02:00 UTC), and purple (24th 06:00 UTC).**

https://doi.org/10.5194/egusphere-2026-3025
Preprint. Discussion started: 26 June 2026


First, as the horizontal resolution increases from d02 to d04, the background $w$ along the parcel trajectories becomes weaker, thereby reducing the average transport speed from the sea surface to the cloud base. We decompose $w$ into a 20-point moving average ($\overline{w}_{20pt}$) and a residual component in Figs. 10a-b. Higher resolution leads to lower $\overline{w}_{20pt}$, whereas resolution has only a minimal effect on the residual component, indicating that the weaker $w$ in the higher-resolution simulations is primarily attributable to changes in the mean state rather than in the fluctuations. Figures 10c-d further show that, with increasing resolution, the fraction of parcels embedded in a background ascending environment decreases, whereas the fraction embedded in a background subsiding environment increases. This suggests that, at higher resolutions, parcels are less frequently sustained within background ascent. Figure 10e shows stronger subsidence in the lower and middle layers and weaker positive $w$ aloft in the high-resolution domain than in the low-resolution domain. Figure 10f indicates stronger horizontal divergence below 1 km and stronger horizontal convergence aloft at higher resolutions, which is consistent with the vertical-velocity structure shown in Fig. 10e.

Second, the limitations of simulation duration and domain size further amplify the transport differences among resolutions. When we extend the analysis window to 120 min and expand the spatial coverage to that of domain d03, the cumulative arrival rates increase markedly: d02 rises to 97.83%, an increase of 3.67% relative to the original result, and d03 rises to 93.17%, an increase of 6.87%, leading to reduced differences among various grid spacings.

https://doi.org/10.5194/egusphere-2026-3025
Preprint. Discussion started: 26 June 2026


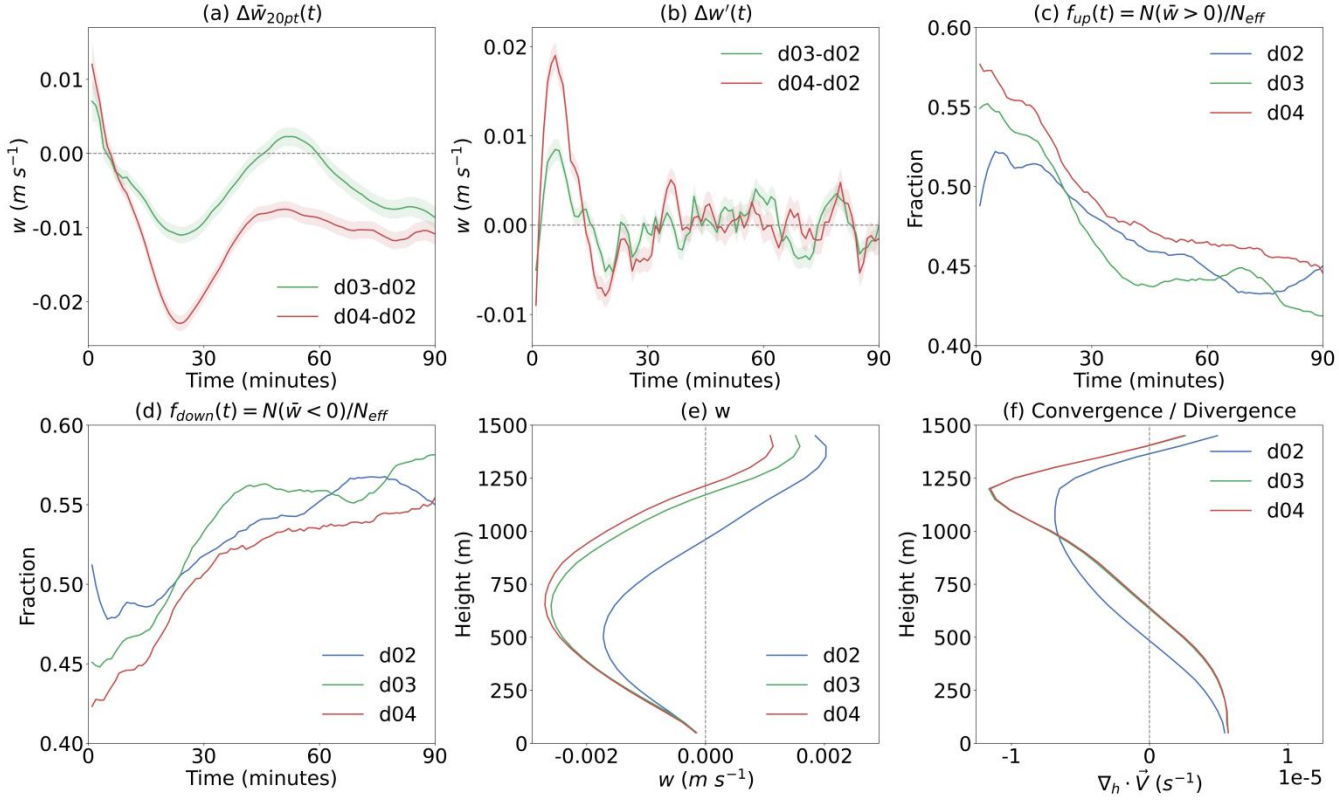


**Figure 10. Vertical transport characteristics and dynamic environmental parameters under different horizontal resolutions. Results are based on the first 90 minutes of simulation starting from 00:00 UTC on the 24th ($t_r = 10$ min). All domain data are cropped to the d04 range for calculation. (a) Difference in the trajectory-sampled background $w$, $\Delta\overline{w}_{20pt}(t)$, where $\overline{w}_{20pt}(t)$ is the background component obtained from a 20-point centered running mean of the trajectory-sampled $w$. (b) Difference in the perturbation $w$, $\Delta w'(t)$. (c) Fraction of parcels in sustained positive background motion, $f_{up}(t) = N(\overline{w} > 0)/N_{eff}$. (d) Fraction of parcels in persistent negative background motion, $f_{down}(t) = N(\overline{w} < 0)/N_{eff}$, where $N_{eff}$ denotes the number of valid parcels at each time. (e) $w$ vertical profile. (f) Convergence / Divergence vertical profile. Negative values on the x-axis represent horizontal convergence, and positive values represent horizontal divergence. The end of the axis is annotated with an order-of-magnitude scaling factor of $10^{-5}$.**

**Table 1. Statistics of parcel transport characteristics under different simulation domains, release times, and simulation durations ($t_r = 10$ min). Statistics include the peak instantaneous arrival rate, peak arrival time, and final cumulative arrival rate. For 90-min simulations, domains d02, d03, and d04 are all cropped to the domain size of d04; for 120-min simulations, d02 and d03 are cropped to the domain size of d03; and the full original d02 domain is used for 180-min simulations.**

https://doi.org/10.5194/egusphere-2026-3025
Preprint. Discussion started: 26 June 2026


| Domain | Start Time | Simulation Duration | Peak | Peak Time | Final Cumulative | Focused Area |
|---|---|---|---|---|---|---|
| d02 | 23 14:00 | 90 min | 2.53% | 15 min | 84.34% | Coverage of d04 |
| | 23 22:00 | | 2.45% | 15 min | 85.68% | Coverage of d04 |
| | 24 00:00 | | 3.39% | 15 min | 94.16% | Coverage of d04 |
| | 24 02:00 | | 2.96% | 15 min | 92.97% | Coverage of d04 |
| | 24 06:00 | | 2.73% | 15 min | 85.50% | Coverage of d04 |
| d03 | 23 14:00 | 90 min | 2.16% | 15 min | 82.00% | Coverage of d04 |
| | 23 22:00 | | 1.90% | 17 min | 77.94% | Coverage of d04 |
| | 24 00:00 | | 2.28% | 16 min | 86.30% | Coverage of d04 |
| | 24 02:00 | | 2.25% | 15 min | 83.87% | Coverage of d04 |
| | 24 06:00 | | 2.06% | 17 min | 79.97% | Coverage of d04 |
| d04 | 23 14:00 | 90 min | 1.84% | 17 min | 75.00% | Coverage of d04 |
| | 23 22:00 | | 1.55% | 19 min | 71.89% | Coverage of d04 |
| | 24 00:00 | | 1.86% | 17 min | 79.70% | Coverage of d04 |
| | 24 02:00 | | 1.80% | 20 min | 76.02% | Coverage of d04 |
| | 24 06:00 | | 1.70% | 19 min | 71.80% | Coverage of d04 |
| d02 | 23 14:00 | 120 min | 2.53% | 15 min | 91.20% | Coverage of d03 |
| | 23 22:00 | | 2.45% | 15 min | 92.07% | Coverage of d03 |
| | 24 00:00 | | 3.39% | 15 min | 97.83% | Coverage of d03 |
| | 24 02:00 | | 2.96% | 15 min | 97.13% | Coverage of d03 |
| | 24 06:00 | | 2.73% | 15 min | 90.72% | Coverage of d03 |
| d03 | 23 14:00 | 120 min | 2.16% | 15 min | 89.35% | Coverage of d03 |
| | 23 22:00 | | 1.90% | 17 min | 87.03% | Coverage of d03 |
| | 24 00:00 | | 2.28% | 16 min | 93.17% | Coverage of d03 |
| | 24 02:00 | | 2.25% | 15 min | 91.37% | Coverage of d03 |
| | 24 06:00 | | 2.06% | 17 min | 89.30% | Coverage of d03 |

425

https://doi.org/10.5194/egusphere-2026-3025
Preprint. Discussion started: 26 June 2026


In addition to the instantaneous and cumulative arrival rates, we investigate the sensitivity of in-cloud residence time to horizontal grid spacing. Figure 11 presents the boxplots of in-cloud residence time for the d02, d03, and d04 domains at two representative release times (14:00 UTC on the 23rd and 00:00 UTC on the 24th) within the 90-min window for the $t_r = 10\ \mathrm{min}$ group. The results indicate that decreasing grid spacing leads to a reduction in in-cloud residence time. For the release at 00:00 UTC on the 24th, the median residence time is 18 min in d02, which decreases to 14 min in d03 and further to 12 min in d04. Enhanced TKE at the cloud top likely contributes to this accelerated venting of parcels from the cloud. Notably, despite the decreasing medians, the high-resolution simulation (d04) captures more prominent extreme outliers at the upper end of the distribution. At 14:00 UTC on the 23rd, the maximum residence time reaches 76 min in d04, exceeding 70 min in d02 and 67 min in d03. While enhanced turbulence reduces the average residence time, strong TKE may also retain a small fraction of parcels for long periods. Both the mean-state and tail-state behaviors may influence droplet activation.

These results indicate that parcel transport to the cloud base, as characterized by the instantaneous arrival rate and cumulative arrival rate, is jointly regulated by release duration, LWP evolution stage, and horizontal resolution, with significant differences in in-cloud residence time. These characteristics provide important constraints on the timing, likelihood, and thermodynamic conditions of subsequent aerosol activation.

https://doi.org/10.5194/egusphere-2026-3025
Preprint. Discussion started: 26 June 2026


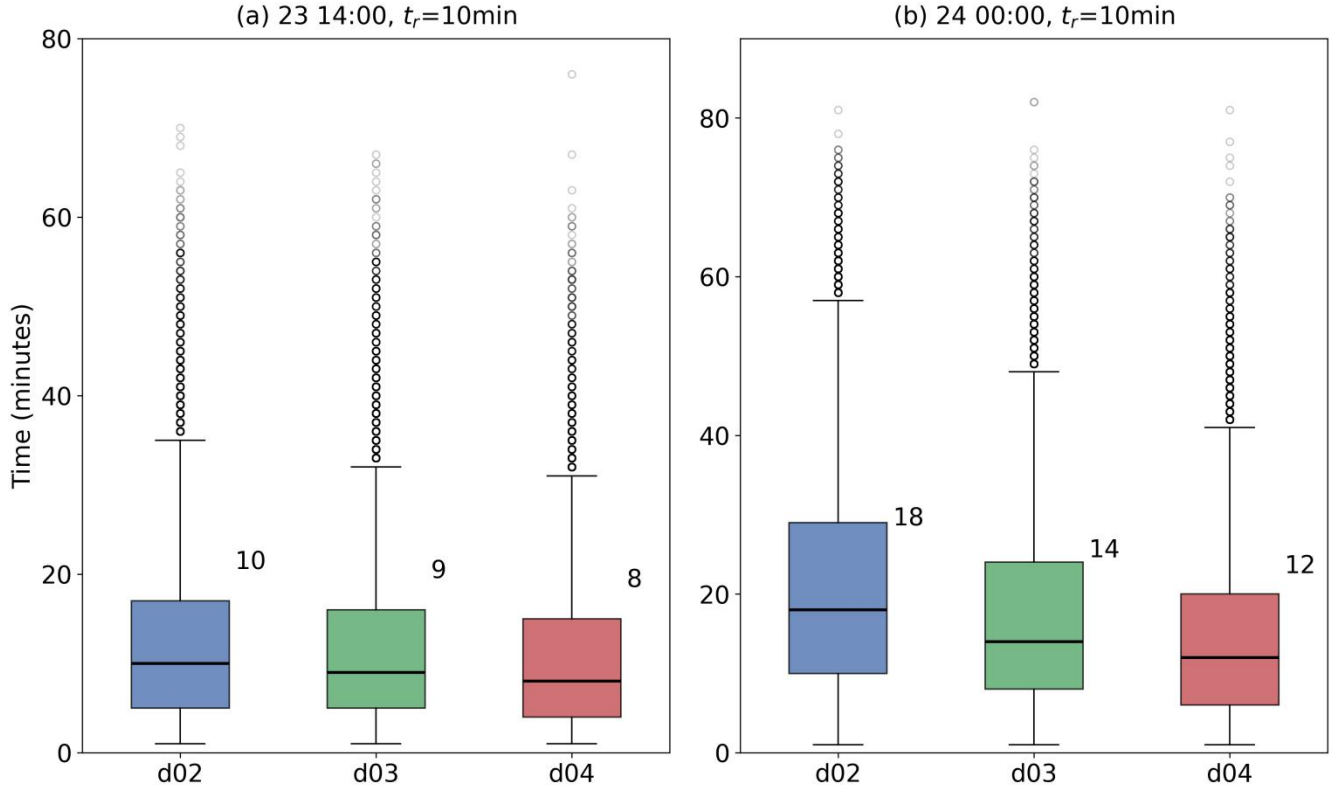


**Figure 11. Boxplot statistics of in-cloud residence time across d02, d03, and d04 domains. Panels (a) and (b) correspond to the release times at 14:00 UTC on the 23rd and 00:00 UTC on the 24th, respectively, for the $t_r = 10\ min$ group within a 90-min window. The blue, green, and red boxes represent results from the d02, d03, and d04 domains, respectively. For consistency in spatial comparison, all data from the d02 and d03 domains are cropped to match the geographical extent of the d04 domain. The central black horizontal line represents the median (numerical values are labeled above each box), while the boxes represent the IQR. Whiskers extend to the maximum and minimum values within the non-outlier range. Black open circles represent outliers, defined as data points exceeding 1.5 times the IQR from the box edges.**

https://doi.org/10.5194/egusphere-2026-3025
Preprint. Discussion started: 26 June 2026


### 3.4 Implications for Droplet Activation

In addition to transport efficiency and in-cloud residence time, quantifying the AF at cloud base is necessary to close the pathway from sea-surface aerosol emissions to cloud droplet formation, particularly under turbulent conditions. The AF used here is a conditional metric rather than a bulk fraction based on all released parcels. Specifically, AF represents the fraction of parcels that activate among those parcels that reach the cloud-base activation layer and are moving upward under the prescribed aerosol conditions. To this end, we evaluate cloud droplet activation using the widely adopted parameterization of Abdul-Razzak and Ghan (1998).

In the estimation of AF, the physicochemical properties of sea-salt aerosols are prescribed as follows: molecular weight $M_a = 0.05844\ \mathrm{kg\ mol^{-1}}$, density $\rho_a = 2200\ \mathrm{kg\ m^{-3}}$ (Koepke et al. 1997; Hess et al. 1998), and geometric standard deviation $\sigma_g = 2.03$ (Koepke et al. 1997; Hess et al. 1998; Jaeglé et al. 2011). A two-dimensional 30×30 parameter space is constructed to cover a wide range of conditions, in which the geometric mean diameter ($D_g$) spans from $0.02 - 5\mu m$ with logarithmic spacing (Quinn et al. 2017), and the aerosol number concentration ($N_a$) ranges from $10 - 5000\ \mathrm{cm^{-3}}$, representing both clean and polluted marine environments (Quinn et al., 2017; O'Dowd and de Leeuw, 2007).

We calculate AF using $w$, temperature ($T$), and pressure ($P$) sampled from Lagrangian particle trajectories over a 90-minute period following release within the spatial coverage of d04. The cloud-base activation layer is defined as the height range extending 50 m above and below the level at which RH exceeds 100%. For each trajectory, samples with negative w within this layer are excluded. The sampled variables within the activation height range are then used in Eq. (30) of Abdul-Razzak and Ghan (1998) to compute the activation ratio for a given aerosol spectrum (characterized by $D_g$ and $N_a$). The mean AF, shown in Fig. 12, is obtained by averaging the activation ratios across all qualified trajectories.

Overall, the AF increases with larger $D_g$ and smaller $N_a$ (Fig. 12a). This trend is expected because larger particles require lower critical supersaturation to activate, while lower $N_a$ tends to lead to higher supersaturation, further enhancing the AF (Chen et al., 2016, 2018). Differences in AF between the two release durations ($t_r = 60\ \mathrm{min}$ and $t_r = 10\ \mathrm{min}$) are minimal (Fig. 12b). However, release timing has a notable impact: releasing at 00:00 leads to a higher AF than releasing at 14:00 (Fig. 12c). This indicates that injecting aerosols when LWP is high enhances activation (Fig. 12c), likely because w is stronger at 00:00 (Fig. 13). High-resolution simulations yield a higher AF than low-resolution ones (Fig. 12d). Specifically, AF in the coarse-resolution domain (d02) fluctuates between 0.73 and 0.91, whereas the high-resolution domain (d04) maintains a stable range of 0.92-0.96. This is likely because higher resolution resolves higher $w$ (Fig. 13b), which enhances AF.

https://doi.org/10.5194/egusphere-2026-3025
Preprint. Discussion started: 26 June 2026


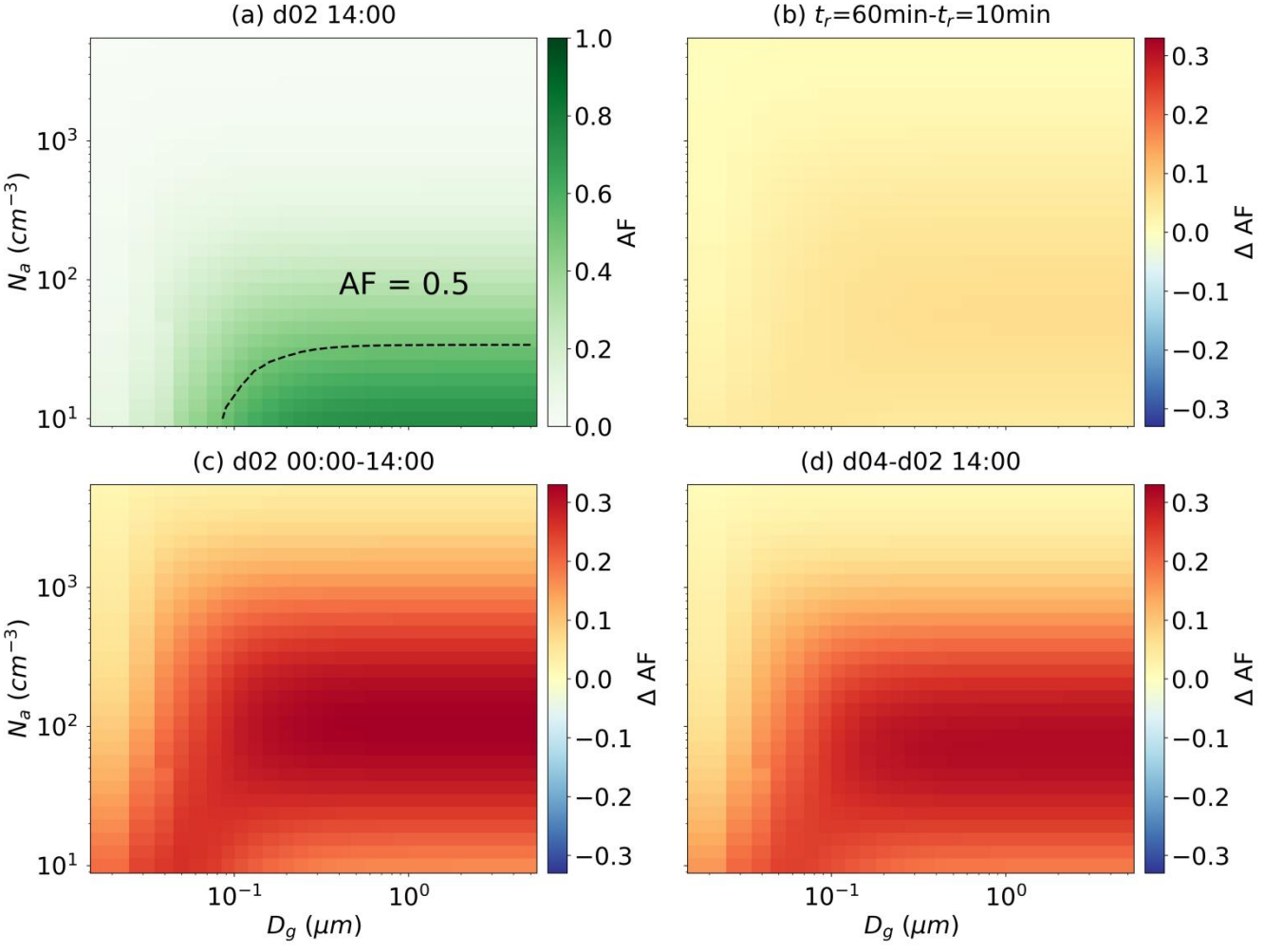


**Figure 12. Sensitivity of the AF and its deviations ($\Delta AF$) for single-mode sea-salt aerosols to grid resolution, release time, and release duration, shown as a function of aerosol $D_{pg}$ and $N_a$. (a) Absolute AF distribution in d02 at 14:00 UTC on the 23rd for $t_r = 10$ min; the black dashed line indicates the AF = 0.5 contour. The "Greens" color scale represents AF values from 0 to 1. (b) $\Delta AF$ in d02 at 14:00 UTC on the 23rd between $t_r = 60$ min and $t_r = 10$ min. (c) $\Delta AF$ in d02 between 00:00 UTC on the 24th and 14:00 UTC on the 23rd for $t_r = 10$ min. (d) $\Delta AF$ between d04 and d02 at 14:00 UTC on the 23rd. The "RdYlBu_r" color scale (red/blue for positive/negative deviations) represents differences in AF.**

https://doi.org/10.5194/egusphere-2026-3025
Preprint. Discussion started: 26 June 2026


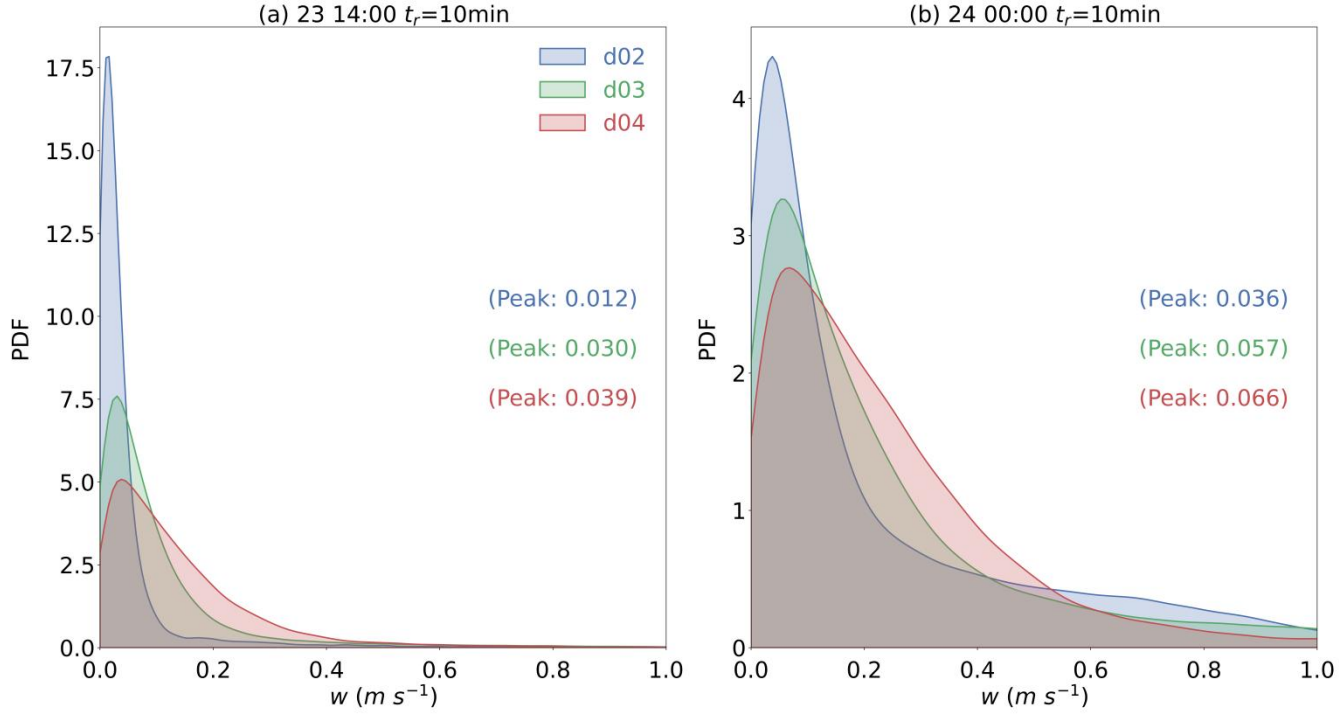


**Figure 13. PDFs of the sampled cloud-base $w$ used for activation diagnostics. (a) Comparison of w distributions across d02, d03, and d04 at 14:00 UTC on the 23rd ($t_r = 10$ min); (b) Comparison of $w$ distributions at 00:00 UTC on the 24th ($t_r = 10$ min). Values in parentheses indicate the peak positions of the respective PDF curves. Blue, green, and red curves represent the results for d02, d03, and d04, respectively.**

https://doi.org/10.5194/egusphere-2026-3025
Preprint. Discussion started: 26 June 2026


## 4 Conclusions

This study investigates key uncertainties in MCB feasibility, focusing on a typical stratocumulus region in the tropical Southeast Atlantic. By coupling WRF-LES with the FLEXPART-WRF Lagrangian particle dispersion model, we quantify the transport characteristics of turbulent parcels from the sea surface to the cloud base, including the instantaneous arrival rate, cumulative arrival rate, transport time, in-cloud residence time, and the potential implications of these transport pathways for cloud droplet activation. The main findings are as follows:

(1) The four-level one-way nested WRF simulation (grid spacing from 2.7 km to 100 m) effectively reproduces the spatiotemporal distribution and evolutionary characteristics of LWP in the study area. The results show good agreement with MODIS satellite observations and significantly mitigate the underestimation of marine stratocumulus LWP in ERA5 reanalysis, thereby providing a reliable meteorological background for the subsequent Lagrangian particle trajectory analysis.

(2) The thermodynamic structure of the boundary layer in the study region is generally uniform; however, turbulence intensity varies markedly across different stages of LWP evolution. Stronger boundary-layer turbulent mixing occurs during the LWP peak and rapid-growth phase. The timing of turbulent parcel release influences the height and thickness of the supersaturated layer as well as the TKE experienced by the parcels, thereby modulating their transport to the cloud base and the subsequent activation conditions.

(3) Turbulent parcel transport to the cloud base, as characterized by the instantaneous arrival rate and cumulative arrival rate, is jointly controlled by release duration, release timing, and horizontal resolution. Short-pulse releases ($t_r = 10$ min) produce higher peak instantaneous arrival rates, whereas continuous releases ($t_r = 60$ min) are characterized by lower peaks and more delayed arrival times; overall transport to the cloud base is stronger during the LWP peak and rapid-growth stages than during low-LWP periods. As the horizontal resolution increases from d02 (900 m) to d04 (100 m), the peak instantaneous arrival rate decreases, the peak arrival time is delayed, and the cumulative arrival rate diagnosed within the analyzed window also decreases overall. This is mainly because the background mean ascent experienced by the parcels weakens at higher resolution, while the truncation effect associated with limited integration time and domain size becomes stronger for slowly rising and later-arriving parcels, thereby jointly reducing the diagnosed overall transport to the cloud base within the analyzed window.

(4) In-cloud residence time and cloud-base activation processes are also sensitive to model resolution. Strong turbulence and abundant water vapor favor longer in-cloud residence times of turbulent parcels. With increasing resolution, the average in-cloud residence time shortens, yet extreme long-residence events become more frequent. Based on simplified single-mode sea-salt aerosol experiments, the cloud droplet AF increases significantly with increasing particle size and decreasing

https://doi.org/10.5194/egusphere-2026-3025
Preprint. Discussion started: 26 June 2026


number concentration, while remaining insensitive to release duration. High-resolution simulations yield higher AF because they better resolve strong cloud-base updrafts.

In summary, this study reveals, from a Lagrangian viewpoint, the transport characteristics of turbulent parcels from the sea surface to the cloud base within the marine boundary layer, as well as the modulating effects of release conditions, horizontal resolution, and in-cloud dynamical environments on activation-relevant conditions at the cloud base. These results provide process-level constraints for assessing MCB release strategies, selecting appropriate model resolutions, and evaluating both the likelihood of injected aerosols reaching the cloud base and the potential brightening implications. It should be noted that the current analysis is based primarily on a single case with limited simulation duration and spatial coverage, together with a simplified single-mode sea-salt aerosol assumption. In particular, the small domain size of d04 causes some parcels to exit the lateral boundaries before reaching the cloud base. Restricting the cross-resolution comparison to the first 90 min may affect the absolute magnitude of the cumulative arrival rate, especially at higher resolutions where parcels rise more slowly and arrive later. Nevertheless, the consistent reductions in peak instantaneous arrival rate, the delayed peak arrival time, and the lower cumulative arrival rate at higher resolution highlight the sensitivity of diagnosed parcel transport to model resolution, release configuration, and the evolving boundary-layer environment. Constraining the key physical uncertainties in the MCB transport-residence-activation chain will require future research to extend this analysis to multi-region, multi-season statistical analyses, employ larger domains or periodic boundary conditions, and incorporate more sophisticated multi-modal parcel models for better simulation of aerosol-cloud interactions.

https://doi.org/10.5194/egusphere-2026-3025
Preprint. Discussion started: 26 June 2026


## Code and data availability

The ERA5 reanalysis data used in this study are available from the Copernicus Climate Data Store (https://cds.climate.copernicus.eu/). The MODIS satellite data were obtained from the National Aeronautics and Space Administration (NASA) via their official data portal (https://modis.gsfc.nasa.gov/). The FLEXPART-WRF model code employed for Lagrangian particle dispersion simulations is publicly accessible at the NILU Git repository (https://git.nilu.no/flexpart/flexpart-wrf/). A subset of analyzed data and post-processing python code are also available from Zenodo (https://zenodo.org/records/20394773).

## Author contributions

Conceptualization: Jingyi Chen
Data curation: Pan Zhao, Jingyi Chen
Formal analysis: Jingyi Chen, Pan Zhao
Funding acquisition: Yang Yang, Jingyi Chen
Investigation: Pan Zhao, Jingyi Chen
Methodology: Jingyi Chen, Pan Zhao
Project administration: Jingyi Chen, Yang Yang
Resources: Yue Jia, Pan Zhao, Jingyi Chen, Yu Yang
Software: Pan Zhao, Jingyi Chen, Yue Jia
Supervision: Jingyi Chen
Validation: Pan Zhao, Jingyi Chen, Yang Yang
Visualization: Pan Zhao
Writing (original draft preparation): Pan Zhao
Writing (review and editing): Jingyi Chen, Yang Yang, Yue Jia

## Competing interests

The authors declare that they have no competing interests.

https://doi.org/10.5194/egusphere-2026-3025
Preprint. Discussion started: 26 June 2026


**Acknowledgements**

We acknowledge the High-Performance Computing Center of Nanjing University of Information Science & Technology for its support of this work. We thank Colleen Kaul for insightful discussions and inspiring perspectives on this topic.

**Financial support**

This study was supported by the National Key Research and Development Program of China (grant 2024YFF0811400), the National Natural Science Foundation of China (Grant No. 42405076), the Startup Foundation for Introducing Talent of NUIST (Grant No. 2024r099), and the Distinguished Young Scholars Program of the National Natural Science Foundation of China (Overseas).

**References**

Abdul-Razzak, H., Ghan, S. J., and Rivera-Carpio, C.: A parameterization of aerosol activation: 1. Single aerosol type, J. Geophys. Res. Atmos., 103, 6123–6131, https://doi.org/10.1029/97JD03735, 1998.

Abdul-Razzak, H. and Ghan, S. J.: A parameterization of aerosol activation: 2. Multiple aerosol types, J. Geophys. Res. Atmos., 105, 6837–6844, https://doi.org/10.1029/1999JD901161, 2000.

Ahlm, L., Jones, A., Stjern, C. W., Muri, H., Kravitz, B., and Kristjánsson, J. E.: Marine cloud brightening – as effective without clouds, Atmos. Chem. Phys., 17, 13071–13087, https://doi.org/10.5194/acp-17-13071-2017, 2017.

Arbizu-Barrena, C., Pozo-Vázquez, D., Ruiz-Arias, J. A., and Tovar-Pescador, J.: Macroscopic cloud properties in the WRF NWP model: An assessment using sky camera and ceilometer data, J. Geophys. Res. Atmos., 120, 10297–10312, https://doi.org/10.1002/2015JD023502, 2015.

Bower, K., Choularton, T., Latham, J., Sahraei, J., and Salter, S.: Computational assessment of a proposed technique for global warming mitigation via albedo-enhancement of marine stratocumulus clouds, Atmos. Res., 82, 328–336, https://doi.org/10.1016/j.atmosres.2005.11.013, 2006.

Brioude, J., Arnold, D., Stohl, A., Cassiani, M., Morton, D., Seibert, P., Angevine, W., Evan, S., Dingwell, A., Fast, J. D., Easter, R. C., Pisso, I., Burkhart, J., and Wotawa, G.: The Lagrangian particle dispersion model FLEXPART-WRF version 3.1, Geosci. Model Dev., 6, 1889–1904, https://doi.org/10.5194/gmd-6-1889-2013, 2013.

Chen, J., Liu, Y., Zhang, M., and Peng, Y.: New understanding and quantification of the regime dependence of aerosol-cloud interaction for studying aerosol indirect effects, Geophys. Res. Lett., 43, 1780–1787, https://doi.org/10.1002/2016GL067683, 2016.

Chen, J., Liu, Y., Zhang, M., and Peng, Y.: Height Dependency of Aerosol-Cloud Interaction Regimes, J. Geophys. Res. Atmos., 123, 491–506, https://doi.org/10.1002/2017JD027431, 2018.

https://doi.org/10.5194/egusphere-2026-3025
Preprint. Discussion started: 26 June 2026


Dhandapani, C., Kaul, C. M., Pressel, K. G., Blossey, P. N., Wood, R., and Kulkarni, G.: Sensitivities of Large Eddy Simulations of Aerosol Plume Transport and Cloud Response, J. Adv. Model. Earth Syst., 17, e2024MS004546, https://doi.org/10.1029/2024MS004546, 2025.

Diamond, M. S., Director, H. M., Eastman, R., Possner, A., and Wood, R.: Substantial Cloud Brightening From Shipping in Subtropical Low Clouds, AGU Adv., 1, e2019AV000111, https://doi.org/10.1029/2019AV000111, 2020.

Diamond, M. S., Gettelman, A., Lebsock, M. D., McComiskey, A., Russell, L. M., Wood, R., and Feingold, G.: To assess marine cloud brightening's technical feasibility, we need to know what to study—and when to stop, Proc. Natl. Acad. Sci. USA, 119, e2118379119, https://doi.org/10.1073/pnas.2118379119, 2022.

Fast, J. D., Gustafson, W. I., Easter, R. C., Zaveri, R. A., Barnard, J. C., Chapman, E. G., Grell, G. A., and Peckham, S. E.: Evolution of ozone, particulates, and aerosol direct radiative forcing in the vicinity of Houston using a fully coupled meteorology-chemistry-aerosol model, J. Geophys. Res. Atmos., 111, D22205, https://doi.org/10.1029/2005JD006721, 2006.

Feingold, G., Ghate, V. P., Russell, L. M., Blossey, P., Cantrell, W., Christensen, M. W., Diamond, M. S., Gettelman, A., Glassmeier, F., Gryspeerdt, E., Haywood, J., Hoffmann, F., Kaul, C. M., Lebsock, M., McComiskey, A. C., McCoy, D. T., Ming, Y., Mülmenstädt, J., Possner, A., Prabhakaran, P., Quinn, P. K., Schmidt, K. S., Shaw, R. A., Singer, C. E., Sorooshian, A., Toll, V., Wan, J. S., Wood, R., Yang, F., Zhang, J., and Zheng, X.: Physical science research needed to evaluate the viability and risks of marine cloud brightening, Sci. Adv., 10, eadi8594, https://doi.org/10.1126/sciadv.adi8594, 2024.

Fountoukis, C. and Nenes, A.: Continued development of a cloud droplet formation parameterization for global climate models, J. Geophys. Res. Atmos., 110, D11212, https://doi.org/10.1029/2004JD005591, 2005.

Glassmeier, F., Hoffmann, F., Johnson, J. S., Yamaguchi, T., Carslaw, K. S., and Feingold, G.: Aerosol-cloud-climate cooling overestimated by ship-track data, Science, 371, 485–489, https://doi.org/10.1126/science.abd3980, 2021.

Grabowski, W. W. and Wang, L.-P.: Growth of Cloud Droplets in a Turbulent Environment, Annu. Rev. Fluid Mech., 45, 293–324, https://doi.org/10.1146/annurev-fluid-011212-140750, 2013.

Hanna, S. R., Briggs, G. A., and Hosker, R. P.: Handbook on atmospheric diffusion, US Dept. of Energy, Springfield, Va, 102 pp., 1982.

Hernandez-Jaramillo, D. C., Harrison, L., Kelaher, B., Ristovski, Z., and Harrison, D. P.: Evaporative Cooling Does Not Prevent Vertical Dispersion of Effervescent Seawater Aerosol for Brightening Clouds, Environ. Sci. Technol., 57, 20559–20570, https://doi.org/10.1021/acs.est.3c04793, 2023.

Hersbach, H., Bell, B., Berrisford, P., Hirahara, S., Horányi, A., Muñoz-Sabater, J., Nicolas, J., Peubey, C., Radu, R., Schepers, D., Simmons, A., Soci, C., Abdalla, S., Abellan, X., Balsamo, G., Bechtold, P., Biavati, G., Bidlot, J., Bonavita, M., De Chiara, G., Dahlgren, P., Dee, D., Diamantakis, M., Dragani, R., Flemming, J., Forbes, R., Fuentes, M., Geer, A., Haimberger, L., Healy, S., Hogan, R. J., Hólm, E., Janisková, M., Keeley, S., Laloyaux, P., Lopez, P., Lupu, C., Radnoti, G., De Rosnay, P., Rozum, I., Vamborg, F., Villaume, S., and Thépaut, J.: The ERA5 global reanalysis, Q. J. R. Meteorol. Soc., 146, 1999–2049, https://doi.org/10.1002/qj.3803, 2020.

https://doi.org/10.5194/egusphere-2026-3025
Preprint. Discussion started: 26 June 2026


Hess, M., Koepke, P., and Schult, I.: Optical properties of aerosols and clouds: The software package OPAC, Bull. Am. Meteorol. Soc., 79, 831–844, https://doi.org/10.1175/1520-0477(1998)079<0831:OPOAAC>2.0.CO;2, 1998.

Hoffmann, F. and Feingold, G.: Cloud Microphysical Implications for Marine Cloud Brightening: The Importance of the Seeded Particle Size Distribution, J. Atmos. Sci., 78, 3247–3262, https://doi.org/10.1175/JAS-D-21-0077.1, 2021.

Hoffmann, F., Mayer, B., and Feingold, G.: A parameterization of interstitial aerosol extinction and its application to marine cloud brightening, J. Atmos. Sci., 79, 2849–2862, https://doi.org/10.1175/JAS-D-22-0047.1, 2022.

Iacono, M. J., Delamere, J. S., Mlawer, E. J., Shephard, M. W., Clough, S. A., and Collins, W. D.: Radiative forcing by long-lived greenhouse gases: Calculations with the AER radiative transfer models, J. Geophys. Res. Atmos., 113, D13103, https://doi.org/10.1029/2008JD009944, 2008.

Jaeglé, L., Quinn, P. K., Bates, T. S., Alexander, B., and Lin, J.-T.: Global distribution of sea salt aerosols: new constraints from in situ and remote sensing observations, Atmos. Chem. Phys., 11, 3137–3157, https://doi.org/10.5194/acp-11-3137-2011, 2011.

Janjić, Z. I.: The step-mountain eta coordinate model: Further developments of the convection, viscous sublayer, and turbulence closure schemes, Mon. Weather Rev., 122, 927–945, 1994.

Jenkins, A. K. L. and Forster, P. M.: The inclusion of water with the injected aerosol reduces the simulated effectiveness of marine cloud brightening, Atmos. Sci. Lett., 14, 164–169, https://doi.org/10.1002/asl2.434, 2013.

Jia, Y., Tegtmeier, S., Atlas, E., and Quack, B.: How marine emissions of bromoform impact the remote atmosphere, Atmos. Chem. Phys., 19, 11089–11103, https://doi.org/10.5194/acp-19-11089-2019, 2019.

Koepke, P., Hess, M., Schult, I., and Shettle, E. P.: Global aerosol data set, https://doi.org/10.17617/2.3365749, 1997.

Latham, J.: Control of global warming?, Nature, 347, 339–340, https://doi.org/10.1038/347339b0, 1990.

Latham, J., Bower, K., Choularton, T., Coe, H., Connolly, P., Cooper, G., Craft, T., Foster, J., Gadian, A., Galbraith, L., Iacovides, H., Johnston, D., Launder, B., Leslie, B., Meyer, J., Neukermans, A., Ormond, B., Parkes, B., Rasch, P., Rush, J., Salter, S., Stevenson, T., Wang, H., Wang, Q., and Wood, R.: Marine cloud brightening, Philos. Trans. R. Soc. A, 370, 4217–4262, https://doi.org/10.1098/rsta.2012.0086, 2012.

Matheou, G. and Teixeira, J.: Sensitivity to Physical and Numerical Aspects of Large-Eddy Simulation of Stratocumulus, Mon. Weather Rev., 147, 2621–2639, https://doi.org/10.1175/MWR-D-18-0294.1, 2019.

Morales Betancourt, R. and Nenes, A.: Understanding the contributions of aerosol properties and parameterization discrepancies to droplet number variability in a global climate model, Atmos. Chem. Phys., 14, 4809–4826, https://doi.org/10.5194/acp-14-4809-2014, 2014.

Nenes, A., Ghan, S., Abdul-Razzak, H., Chuang, P. Y., and Seinfeld, J. H.: Kinetic limitations on cloud droplet formation and impact on cloud albedo, Tellus B, 53, 133–149, https://doi.org/10.1034/j.1600-0889.2001.d01-12.x, 2001.

O'Dowd, C. D. and de Leeuw, G.: Marine aerosol production: a review of the current knowledge, Philos. Trans. R. Soc. A, 365, 1753–1774, https://doi.org/10.1098/rsta.2007.2043, 2007.

https://doi.org/10.5194/egusphere-2026-3025
Preprint. Discussion started: 26 June 2026


Peng, Y., Lohmann, U., and Leaitch, R.: Importance of vertical velocity variations in the cloud droplet nucleation process of marine stratus clouds, J. Geophys. Res. Atmos., 110, D21202, https://doi.org/10.1029/2004JD004922, 2005.

Prabhakaran, P., Hoffmann, F., and Feingold, G.: Evaluation of Pulse Aerosol Forcing on Marine Stratocumulus Clouds in the Context of Marine Cloud Brightening, J. Atmos. Sci., 80, 1585–1604, https://doi.org/10.1175/JAS-D-22-0207.1, 2023.

Quinn, P. K., Coffman, D. J., Johnson, J. E., Upchurch, L. M., and Bates, T. S.: Small fraction of marine cloud condensation nuclei made up of sea spray aerosol, Nat. Geosci., 10, 674–679, https://doi.org/10.1038/ngeo3003, 2017.

Rasch, P. J., Hirasawa, H., Wu, M., Doherty, S. J., Wood, R., Wang, H., Jones, A., Haywood, J., and Singh, H.: A protocol for model intercomparison of impacts of marine cloud brightening climate intervention, Geosci. Model Dev., 17, 7963–7994, https://doi.org/10.5194/gmd-17-7963-2024, 2024.

Russell, L. M., Seinfeld, J. H., Flagan, R. C., Ferek, R. J., Hegg, D. A., Hobbs, P. V., Wobrock, W., Flossmann, A. I., O'Dowd, C. D., Nielsen, K. E., and Durkee, P. A.: Aerosol dynamics in ship tracks, J. Geophys. Res. Atmos., 104, 31077–31095, https://doi.org/10.1029/1999JD900985, 1999.

Skamarock, W. C., Klemp, J. B., Dudhia, J., Gill, D. O., Liu, Z., Berner, J., Wang, W., Powers, J. G., Duda, M. G., Barker, D. M., and Huang, X.-Y.: A Description of the Advanced Research WRF Model Version 4, NCAR Tech. Note NCAR/TN-556+STR, 145 pp., https://doi.org/10.5065/1dfh-6p97, 2019.

Stevens, B.: Entrainment in stratocumulus-topped mixed layers, Q. J. R. Meteorol. Soc., 128, 2663–2690, https://doi.org/10.1256/qj.01.202, 2002.

Stohl, A., Forster, C., Frank, A., Seibert, P., and Wotawa, G.: Technical note: The Lagrangian particle dispersion model FLEXPART version 6.2, Atmos. Chem. Phys., 5, 2461–2474, https://doi.org/10.5194/acp-5-2461-2005, 2005.

Tewari, M., Chen, F., Wang, W., Dudhia, J., LeMone, M. A., Gayno, G., Wegiel, J., and Cuenca, R. H.: Implementation and verification of the unified NOAH land surface model in the WRF model, 20th Conference on Weather Analysis and Forecasting/16th Conference on Numerical Weather Prediction, Seattle, WA, 11–15 January 2004, 11–15, 2004.

Thompson, G., Field, P. R., Rasmussen, R. M., and Hall, W. D.: Explicit Forecasts of Winter Precipitation Using an Improved Bulk Microphysics Scheme. Part II: Implementation of a New Snow Parameterization, Mon. Weather Rev., 136, 5095–5115, https://doi.org/10.1175/2008MWR2387.1, 2008.

VanReken, T. M., Rissman, T. A., Roberts, G. C., Varutbangkul, V., Jonsson, H. H., Flagan, R. C., and Seinfeld, J. H.: Toward aerosol/cloud condensation nuclei (CCN) closure during CRYSTAL-FACE, J. Geophys. Res. Atmos., 108, 4633, https://doi.org/10.1029/2003JD003582, 2003.

Wang, H., Rasch, P. J., and Feingold, G.: Manipulating marine stratocumulus cloud amount and albedo: a process-modelling study of aerosol-cloud-precipitation interactions in response to injection of cloud condensation nuclei, Atmos. Chem. Phys., 11, 4237–4249, https://doi.org/10.5194/acp-11-4237-2011, 2011.

Wood, R.: Stratocumulus Clouds, Mon. Weather Rev., 140, 2373–2423, https://doi.org/10.1175/MWR-D-11-00121.1, 2012.

Wood, R.: Assessing the potential efficacy of marine cloud brightening for cooling Earth using a simple heuristic model, Atmos. Chem. Phys., 21, 14507–14533, https://doi.org/10.5194/acp-21-14507-2021, 2021.

https://doi.org/10.5194/egusphere-2026-3025
Preprint. Discussion started: 26 June 2026


740 Xue, H., Feingold, G., and Stevens, B.: Aerosol Effects on Clouds, Precipitation, and the Organization of Shallow Cumulus Convection, J. Atmos. Sci., 65, 392–406, https://doi.org/10.1175/2007JAS2428.1, 2008.

Zelinka, M. D., Randall, D. A., Webb, M. J., and Klein, S. A.: Clearing clouds of uncertainty, Nat. Clim. Change, 7, 674–678, https://doi.org/10.1038/nclimate3402, 2017.